

A 38 Million Year Old Neptune-Sized Planet in the Kepler Field

² L. G. BOUMA,^{1,2,*} J. L. CURTIS,^{3,4} K. MASUDA,⁵ L. A. HILLENBRAND,¹ G. STEFANSSON,^{2,†} H. ISAACSON,⁶
³ N. NARITA,^{7,8,9,10} A. FUKUI,^{7,10} M. IKOMA,¹¹ M. TAMURA,^{12,9,11} A. L. KRAUS,¹³ E. FURLAN,¹⁴
⁴ C. L. GNILKA,^{15,14} K. V. LESTER,¹⁵ AND S. B. HOWELL¹⁵

⁵ Cahill Center for Astrophysics, California Institute of Technology, Pasadena, CA 91125, USA

⁶ Department of Astrophysical Sciences, Princeton University, 4 Ivy Lane, Princeton, NJ 08540, USA

⁷ Department of Astronomy, Columbia University, 550 West 120th Street, New York, NY 10027, USA

⁸ Department of Astrophysics, American Museum of Natural History, New York, NY 10024, USA

⁹ Department of Earth and Space Science, Osaka University, Osaka 560-0043, Japan

¹⁰ Astronomy Department, University of California, Berkeley, CA 94720, USA

¹¹ Komaba Institute for Science, The University of Tokyo, Tokyo 153-8902, Japan

¹² Japan Science and Technology Agency, PRESTO, Tokyo 153-8902, Japan

¹³ Astrobiology Center, Tokyo 181-8588, Japan

¹⁴ Instituto de Astrofísica de Canarias (IAC), 38205 La Laguna, Tenerife, Spain

¹⁵ Division of Science, National Astronomical Observatory of Japan, Tokyo 181-8588, Japan

¹⁶ Department of Astronomy, The University of Tokyo, Tokyo 113-0033, Japan

¹⁷ Department of Astronomy, The University of Texas at Austin, Austin, TX 78712, USA

¹⁸ NASA Exoplanet Science Institute, Caltech/IPAC, Pasadena, CA 91125, USA

¹⁹ NASA Ames Research Center, Moffett Field, CA 94035, USA

(Received 2021 Oct 12; Revised —; Accepted —)

Submitted to AAS Journals

ABSTRACT

Kepler 1627A is a G8V star previously known to host a $3.8R_{\oplus}$ planet on a 7.2 day orbit. The star was observed by the Kepler space telescope because it is nearby ($d = 329$ pc) and it resembles the Sun. Here we show using Gaia kinematics, TESS stellar rotation periods, and spectroscopic lithium abundances that Kepler 1627 is a member of the 38^{+6}_{-5} Myr old δ Lyr cluster. To our knowledge, this makes Kepler 1627Ab the youngest planet with a precise age yet found by the prime Kepler mission. The Kepler photometry shows two peculiarities: the average transit profile is asymmetric, and the individual transit times might be correlated with the local light curve slope. We discuss possible explanations for each anomaly. More importantly, the δ Lyr cluster is one of $\sim 10^3$ coeval groups whose properties have been clarified by Gaia. Many other exoplanet hosts are candidate members of these clusters; their ages can be verified with the trifecta of Gaia, TESS, and ground-based spectroscopy.

Keywords: exoplanet evolution (491), open star clusters (1160), stellar ages (1581)

1. INTRODUCTION

While thousands of exoplanets have been discovered orbiting nearby stars, the vast majority of them are several billion years old. This makes it

difficult to test origin theories for the different families of planets, since many evolutionary processes are expected to operate on timescales of less than 100 million years.

For instance, the “mini-Neptunes”, thought to be made of metal cores, silicate mantles (Kite et al. 2020), and extended hydrogen-dominated atmospheres, are expected to shrink in size by factors of several over their first 10^8 years. Specifically, in the models of Owen & Wu (2016) and

Corresponding author: L. G. Bouma
luke@astro.caltech.edu

* 51 Pegasi b Fellow

† Henry Norris Russell Fellow

Owen (2020), the $\approx 5 M_{\oplus}$ planets start with sizes of $4-12 R_{\oplus}$ shortly after the time of disk dispersal ($\lesssim 10^7$ years), and shrink to sizes of $2-4 R_{\oplus}$ by 10^8 years. While the majority of this change is expected to occur within the first few million years after the disk disperses (Ikoma & Hori 2012), stellar irradiation and internal heat can also power gradual outflows which, if strong enough, can deplete or entirely strip the atmosphere (Lopez et al. 2012; Owen & Wu 2013; Ginzburg et al. 2018). The latter photoevaporative and core-powered outflows are thought to persist for $\approx 10^8$ to $\approx 10^9$ years, though the details depend on the planetary masses, the irradiation environments, and the initial atmospheric mass fractions (Owen & Wu 2017; Gupta & Schlichting 2020; Rogers & Owen 2021; King & Wheatley 2021). Discovering young planets, measuring their masses, and detecting their atmospheric outflows are key steps toward testing this paradigm, which is often invoked to explain the observed radius distribution of mature exoplanets (Fulton et al. 2017; Van Eylen et al. 2018).

The K2 and TESS missions have now enabled the detection of about ten close-in planets younger than 100 million years, all smaller than Jupiter (Mann et al. 2016; David et al. 2016, 2019; Newton et al. 2019; Bouma et al. 2020; Plavchan et al. 2020; Rizzuto et al. 2020; Martioli et al. 2021). The Kepler mission however has not yielded any planets with precise ages below one gigayear (Meibom et al. 2013). The reason is that during the prime Kepler mission (2009–2013), only four open clusters were known in the Kepler field, with ages spanning 0.7 Gyr to 9 Gyr (Meibom et al. 2011). Though isochronal, gyrochronal, and lithium-based analyses suggest that younger Kepler planets do exist (Walkowicz & Basri 2013; Berger et al. 2018; David et al. 2021), accurate and precise age measurements typically require an ensemble of stars. Fortunately, recent analyses of the Gaia data have greatly expanded our knowledge of cluster memberships (e.g., Cantat-Gaudin et al. 2018; Zari et al. 2018; Kounkel & Covey 2019; Meingast et al. 2021; Kerr et al. 2021). As part of our Cluster Difference Imaging Photometric Survey (CDIPS, Bouma et al. 2019), we concatenated the available analyses from the literature, which yielded a list of candidate young and aged stars (see Appendix A).

Matching our young star list against stars observed by Kepler revealed that Kepler observed a portion of the δ Lyr cluster (Stephenson-1; Theia 73). More specifically, a clustering analysis of the Gaia data by Kounkel & Covey (2019) reported that Kepler 1627 (KIC 6184894; KOI 5245) is a δ Lyr cluster member. Given the previous statistical validation of the close-in Neptune-sized

planet Kepler 1627b (Tenenbaum et al. 2012; Morton et al. 2016; Thompson et al. 2018), we begin by scrutinizing the properties of the cluster (Section 2). We find that the δ Lyr cluster is 38^{+6}_{-5} Myr old, and in Section 3 show that Kepler 1627 is both a binary and also a member of the cluster. Focusing on the planet (Section 4), we confirm that despite the existence of the previously unreported M2.5V companion, hereafter Kepler 1627B, the planet orbits the G-dwarf primary, Kepler 1627A. We also analyze an asymmetry in the average transit profile, and a possible correlation between the individual transit times and the local light curve slope. We conclude by discussing broader implications for our ability to age-date a larger sample of planets (Section 5).

2. THE CLUSTER

To measure the age of the δ Lyr cluster, we first selected a set of candidate cluster members (Section 2.1), and then analyzed these stars using a combination of the isochronal and gyrochronal techniques (Section 2.2).

2.1. Selecting Cluster Members

Kounkel & Covey (2019) applied an unsupervised clustering algorithm to Gaia DR2 on-sky positions, proper motions, and parallaxes for stars within the nearest kiloparsec. For the δ Lyr cluster (Theia 73), they reported 3,071 candidate members. We matched these stars against the latest Gaia EDR3 observations using the dr2_neighbourhood table from the ESA archive, taking the stars closest in proper motion and epoch-corrected angular distance as the presumed match (Gaia Collaboration et al. 2021a). For plotting purposes, we focused only on the stars with parallax signal-to-noise exceeding 20. We calculated the tangential velocities for each of these stars relative to Kepler 1627 ($\Delta\mu^*$) by subtracting the observed proper motion from what the proper motion at each star’s position would be if it were co-moving with Kepler 1627.

Figure 1 shows that the reported cluster members (gray and black points) extend over a much larger volume in both physical and kinematic space than the cluster previously identified by Stephenson (1959) and later corroborated by Eggen (1968). While the non-uniform “clumps” of stars might comprise a *bona fide* cluster of identically-aged stars, they could also be heavily contaminated by field stars. One reason to suspect this is that the spread in tangential velocities exceeds typical limits for kinematic coherence (Meingast et al. 2021). We therefore considered stars only in the immediate kinematic and spatial vicinity of Kepler 1627 as candidate cluster members. We performed this selection cut manually, by drawing lassos with the in-

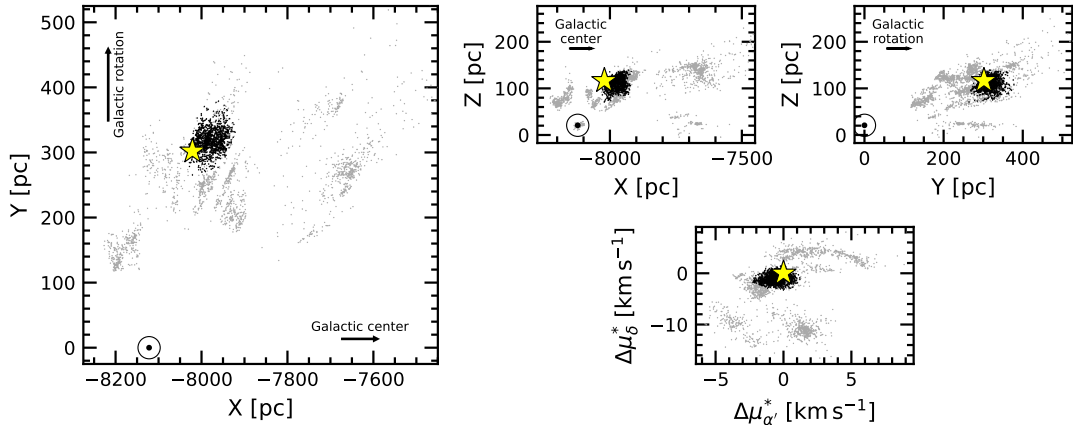


Figure 1. Galactic positions and tangential velocities of stars in the δ Lyr cluster. Points are reported cluster members from Kounkel & Covey (2019). The tangential velocities relative to Kepler 1627 (bottom right) are computed assuming that every star has the same three-dimensional spatial velocity as Kepler 1627. Our analysis considers stars (black points) in the spatial and kinematic vicinity of Kepler 1627 (yellow star). The question of whether the other candidate cluster members (gray points) are part of the cluster is outside our scope. The location of the Sun is (\odot) is shown to clarify the direction along which parallax uncertainties are expected to produce erroneous clusters.

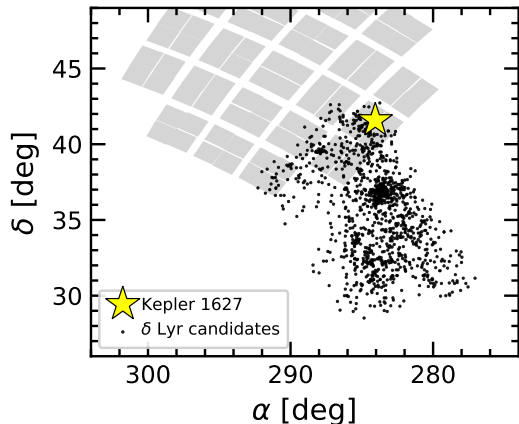


Figure 2. Kepler's view of the δ Lyr cluster, shown in equatorial coordinates. Each black circle is a candidate cluster member selected based on its position and kinematics (Figure 1). Of the 1,201 candidate cluster members, 58 have at least one quarter of Kepler data. TESS has also observed most of the cluster, for one to two lunar months to date.

teractive glue visualization tool (Beaumont et al. 2014) in the four projections shown in Figure 1. The overlap between the Kepler field and the resulting candidate cluster members is shown in Figure 2. While this method will include some field interlopers in the “cluster star” sample, and vice-versa, it should suffice for our aim of verifying the existence of the cluster in the vicinity of Kepler 1627.

2.2. The Cluster’s Age

2.2.1. Color-Absolute Magnitude Diagram

We measured the isochrone age using an empirical approach. The upper left panel of Figure 3 shows the color-absolute magnitude diagram (CMD) of candidate δ Lyr cluster members, IC 2602 (≈ 38 Myr), the Pleiades (≈ 115 Myr), and the field. The stars from the Pleiades and IC 2602 were adopted from Cantat-Gaudin et al. (2018), and the field stars are from the Gaia EDR3 Catalog of Nearby Stars (Gaia Collaboration et al. 2021b). We also compared against μ -Tau (62 ± 7 Myr; Gagné et al. 2020) and the Upper-Centaurus-Lupus (UCL) component of the Sco OB2 association (≈ 16 Myr; Pecaut & Mamajek 2016). We adopted the UCL members from Damiani et al. (2019). For visual clarity, the latter two clusters are not shown in Figure 3. We cleaned the membership lists following the data filtering criteria from Gaia Collaboration et al. (2018a, Appendix B), except that we weakened the parallax precision requirement to $\varpi/\sigma_\varpi > 5$. This also involved cuts on the photometric signal to noise ratio, the number of visibility periods used, the astrometric χ^2 of the single-source solution, and the $G_{\text{BP}} - G_{\text{RP}}$ color excess factor. These filters were designed to include genuine binaries while omitting instrumental artifacts. To correct for extinction, we queried the 3-dimensional maps of Capitanio et al. (2017) and Lallement et al. (2018)¹, and applied the extinction coefficients $k_X \equiv A_X/A_0$ computed by Gaia Collaboration et al. (2018a) assuming that $A_0 = 3.1E(B-V)$. For UCL, IC 2602, the Pleiades, and the δ Lyr cluster, this procedure yielded a respective mean and standard deviation for the reddening of

¹ <https://stilism.obspm.fr/>, 2021/09/25

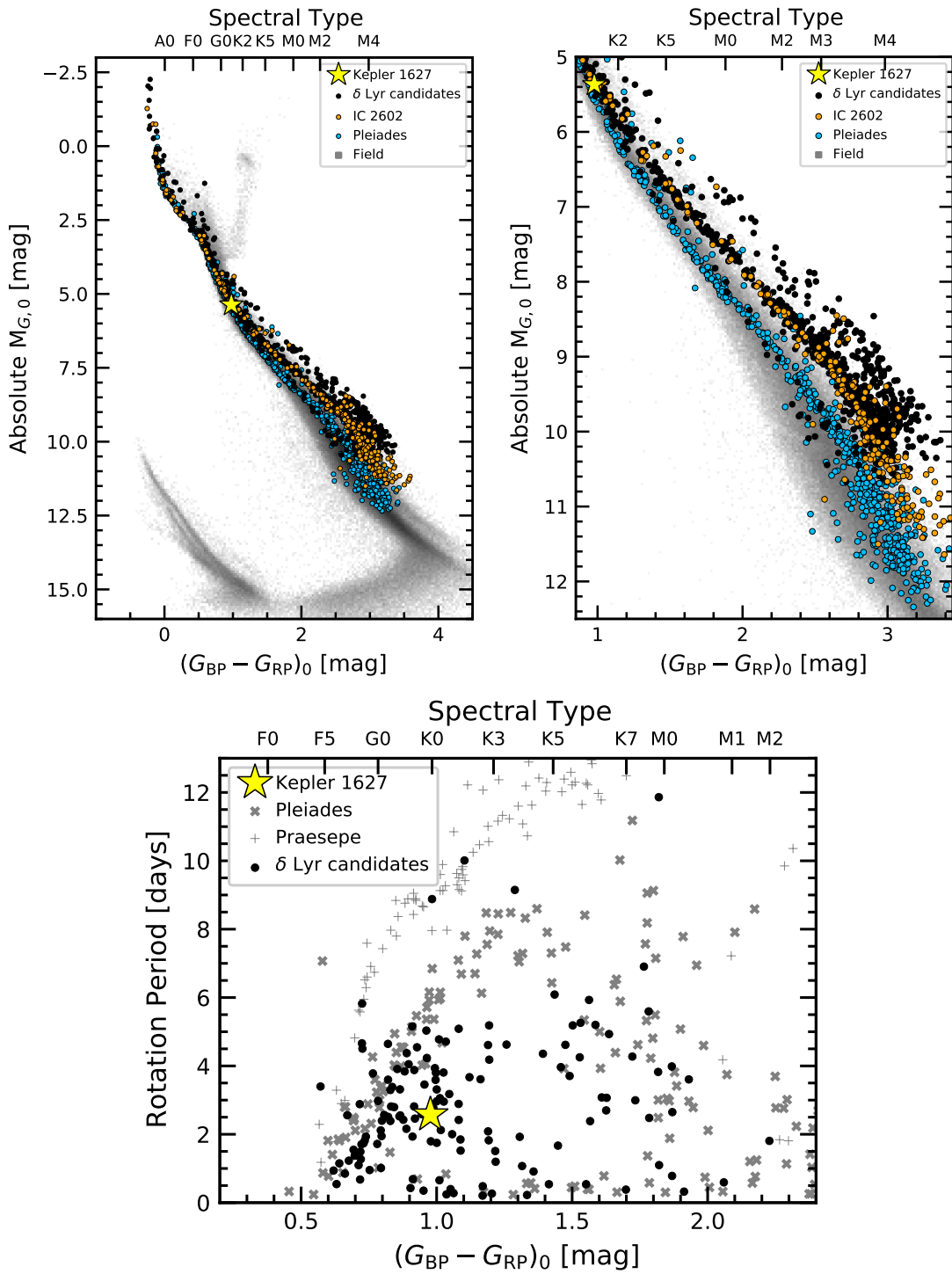


Figure 3. The δ Lyr cluster is 38^{+6}_{-5} Myr old. *Top:* Color-absolute magnitude diagram of candidate δ Lyr cluster members, in addition to stars in IC 2602 (≈ 38 Myr), the Pleiades (≈ 115 Myr), and the Gaia EDR3 Catalog of Nearby Stars (gray background). The zoomed right panel highlights the pre-main-sequence. The δ Lyr cluster and IC 2602 are approximately the same isochronal age. *Bottom:* TESS and Kepler stellar rotation period versus dereddened Gaia color, with the Pleiades and Praesepe (650 Myr) shown for reference (Rebull et al. 2016; Douglas et al. 2017). Most candidate δ Lyr cluster members are gyrochronologically younger than the Pleiades; outliers are probably field interlopers.

$E(B-V) = \{0.084 \pm 0.041, 0.020 \pm 0.003, 0.045 \pm 0.008, 0.032 \pm 0.006\}$. These values are within a factor of two of previously reported values in the literature (Pecaut & Mamajek 2016; Gaia Collaboration et al. 2018a; Kounkel & Covey 2019; Bossini et al. 2019), and are all small enough that the choice of whether to use them vs. other extinction estimates does not affect our primary conclusions.

Figure 3 shows that the δ Lyr cluster and IC 2602 overlap, and therefore are approximately the same age. The pre-main-sequence M dwarfs of the δ Lyr cluster were also seen to be “below” UCL and “above” the Pleiades. To turn this heuristic interpolation into a quantitative age measurement, we used the empirical method developed by Gagné et al. (2020). In brief, we fitted the pre-main-sequence loci of a set of reference clusters, and the locus of the target δ Lyr cluster was then modeled as a piecewise linear combination of these reference clusters. For our reference clusters, we used UCL, IC 2602, and the Pleiades. We removed binaries by requiring RUWE < 1.3, radial_velocity_error below the 80th percentile of each cluster’s distribution, and excluded stars that were obvious photometric binaries in the CAMD.² We then passed a moving box average and standard deviation across the CAMD in 0.10 mag bins, fitted a univariate spline to the binned values, and assembled a piecewise grid of isochrones spanning the ages between UCL and the Pleiades using Equation 6 from Gagné et al. (2020). To derive a probability distribution function for the age of δ Lyr cluster, we then assumed a Gaussian likelihood that treated the interpolated isochrones as the “model” and the δ Lyr cluster’s isochrone as the “data” (Equation 7 from Gagné et al. 2020). The cluster’s age and its statistical uncertainty are then quoted as the the mean and standard deviation of this age posterior.

The ages returned by this procedure depend on the ages assumed for each reference cluster. We adopted a 115 Myr age for the Pleiades (Dahm 2015), and a 16 Myr age for UCL (Pecaut & Mamajek 2016). The age of IC 2602 however is the most important ingredient, since it receives the most weight in the interpolation. Plausible ages for IC 2602 span 30 Myr to 46 Myr, with older ages being preferred by the lithium-depletion-boundary (LDB) measurements (Dobbie et al. 2010; Randich et al. 2018) and younger ages by the main-sequence turn-off (Stauffer et al. 1997; David & Hillenbrand 2015; Bossini et al. 2019). If we were

² For a description of the renormalized unit weight error (RUWE), see the GAIA DPAC technical note http://www.rssd.esa.int/doc_fetch.php?id=3757412.

to adopt the 30 Myr age for IC 2602, then the δ Lyr cluster would be 31^{+5}_{-4} Myr old. For the converse extreme of 46 Myr, the δ Lyr cluster would be 44^{+8}_{-7} Myr old. We adopt an intermediate 38 Myr age for IC 2602, which yields an age for the δ Lyr cluster of 38^{+6}_{-5} Myr.³ Follow-up studies of the LDB or main-sequence turn-off in the δ Lyr cluster could help determine a more precise and accurate age for the cluster, and are left for future work.

2.2.2. Stellar Rotation Periods

Of the 3,071 candidate δ Lyr cluster members reported by Kounkel & Covey (2019), 924 stars were amenable to rotation period measurements ($G < 17$ and $(G_{BP} - G_{RP})_0 > 0.5$) using the TESS full frame image data. As a matter of scope, we restricted our attention to the 391 stars discussed in Section 2.1 in the spatial and kinematic proximity of Kepler 1627. We extracted light curves from the TESS images using the nearest pixel to each star, and regressed them against systematics with the causal pixel model implemented in the unpopular package (Hattori et al. 2021). We then measured candidate rotation periods using a Lomb-Scargle periodogram (Lomb 1976; Scargle 1982; Astropy Collaboration et al. 2018). To enable cuts on crowding, we queried the Gaia source catalog for stars within a 21.⁰ radius of the target star (a radius of 1 TESS pixel). Within this radius, we recorded the number of stars with greater brightness than the target star, and with brightness within 1.25 TESS magnitudes of the target star.

We then cleaned the candidate TESS rotation period measurements through a combination of automated and manual steps. First, to validate the TESS rotation periods, we compared against 28 stars from McQuillan et al. (2014) that were also observed by Kepler. Of the 23 stars with Kepler periods below 10 days, 21 of the TESS periods agreed with the Kepler rotation periods; the other 2 were measured at the double-period harmonic. Of the remaining 5 stars with Kepler rotation periods above 10 days, none were correctly recovered by TESS, and 3 were near the half-period harmonic. We therefore adopted a general stance of skepticism for TESS rotation periods exceeding 10 days, and used the Kepler rotation periods whenever possible. For the remaining stars with only TESS data, we focused only on the stars for which no companions were known with a brightness exceeding one-tenth of the target star in a 21.⁰ radius. There

³ Our exploration of the PARSEC and MIST isochrone models over a grid of ages, metallicities, and reddenings, yielded the best agreement for this ≈ 38 Myr age as well, given $[Fe/H] = +0.1$ and $A_V = 0.2$ (Bressan et al. 2012; Choi et al. 2016); this preferred CAMD reddening is higher than the Lallement et al. (2018) value by a factor of two.

were 192 stars that met these crowding requirements, and that had TESS data available. For plotting purposes we then imposed a selection based on the strength of the signal itself: we required the Lomb Scargle power to exceed 0.2, and the period to be below 15 days.

The lower panel of Figure 3 shows the resulting 145 stars. The majority of these stars fall below the “slow sequence” of the Pleiades, consistent with a gyrochronal age for the δ Lyr cluster below 100 Myr. In fact, the rotation-color distributions of other 30 Myr to 50 Myr clusters (*e.g.*, IC 2602 and IC 2391) are indistinguishable (Douglas et al. 2021). Approximately 10 of the δ Lyr cluster stars appear as outliers above the “slow sequence”. Assuming that they are all false positives (*i.e.*, field interlopers), our rotation period detection fraction would be $135/192 \approx 70\%$. Although some of these outlier stars might be unresolved F+K binaries that are in the cluster (Stauffer et al. 2016), assuming that they are field contaminants provides a more secure lower bound of the rotation period detection fraction. A final possible confounding factor – binarity – is known to affect the “fast sequence” of stars beneath the slow sequence (Meibom et al. 2007; Gillen et al. 2020; Bouma et al. 2021). We do not expect it to change the central conclusion regarding the cluster’s age.

3. THE STARS

3.1. Kepler 1627A

3.1.1. Age

Based on the spatial and kinematic association of Kepler 1627 with the δ Lyr cluster, and the assumption that the planet formed shortly after the star, it seems likely that Kepler 1627 is the same age as the cluster. There are two consistency checks on whether this is true: rotation and lithium. Based on the Kepler light curve, the rotation period is 2.642 ± 0.042 days, where the quoted uncertainty is based on the scatter in rotation periods measured from each individual Kepler quarter. This is consistent with comparable cluster members (Figure 3).

To infer the amount of Li I from the 6708 Å doublet (*e.g.*, Soderblom et al. 2014), we acquired an iodine-free spectrum from Keck/HIRES on the night of 2021 March 26 using the standard setup and reduction techniques of the California Planet Survey (Howard et al. 2010). Following the equivalent width measurement procedure described by Bouma et al. (2021), we find $\text{EW}_{\text{Li}} = 233^{+5}_{-7}$ mÅ. This value does not correct for the Fe I blend at 6707.44 Å. Nonetheless, given the stellar effective temperature (Table 1), this measurement is in agreement with expectations for a ≈ 40 Myr star (*e.g.*, as measured in IC 2602 by Randich et al. 2018). It is also larger than any lithium equivalent

widths measured by Berger et al. (2018) in their analysis of 1,301 Kepler-star spectra.

3.1.2. Stellar Properties

The adopted stellar parameters are listed in Table 1. The stellar mass, radius, and effective temperature are found by interpolating against a 38 Myr MIST isochrone (Choi et al. 2016). The statistical uncertainties are propagated from the absolute magnitude (mostly originating from the parallax uncertainty) and the color; the systematic uncertainties are taken to be the difference between the PARSEC (Bressan et al. 2012) and MIST isochrones. Reported uncertainties are a quadrature sum of the statistical and systematic components. As a consistency check, we analyzed the aforementioned Keck/HIRES spectrum from the night of 2021 March 26 using a combination of SpecMatch-Emp for stellar properties, and SpecMatch-Synth for $v\sin i$ (Yee et al. 2017). This procedure yielded $T_{\text{eff}} = 5498 \pm 100$ K, $\log g = 4.6 \pm 0.1$, $[\text{Fe}/\text{H}] = 0.15 \pm 0.10$ from SpecMatch-Emp, and $v\sin i = 18.9 \pm 1.0$ from SpecMatch-Synth. These values are within the $1-\sigma$ uncertainties of our adopted values from the isochrone interpolation.

3.2. Kepler 1627B

We first noted the presence of a close neighbor in the Kepler 1627 system on 2015 July 22 when we acquired adaptive optics imaging using the NIRC2 imager on Keck-II. We used the narrow camera (FOV = 10.2'') to obtain 8 images in the K' filter ($\lambda = 2.12 \mu\text{m}$) with a total exposure time of 160 s. We analyzed these data following Kraus et al. (2016), which entailed using PSF-fitting to measure the separation, position angle, and contrast of the candidate companion. The best-fitting empirical PSF template was identified from among the near-contemporaneous observations of single stars in the same filter. The mean values inferred from the 8 images are reported in Table 1. To estimate the detection limits, we analyzed the residuals after subtracting the empirical PSF template. Within each residual image, the flux was measured through 40 mas apertures centered on every pixel, and then the noise as a function of radius was estimated from the RMS within concentric rings. Finally, the detection limits were estimated from the strehl-weighted sum of the detection significances in the image stack, and we adopted the $6-\sigma$ threshold as the detection limit for ruling out additional companions.

We also observed Kepler 1627 on Gemini-North using the ‘Alopeke speckle imager on 2021 June 24. ‘Alopeke is a dual-channel speckle interferometer that uses narrow-band filters centered at

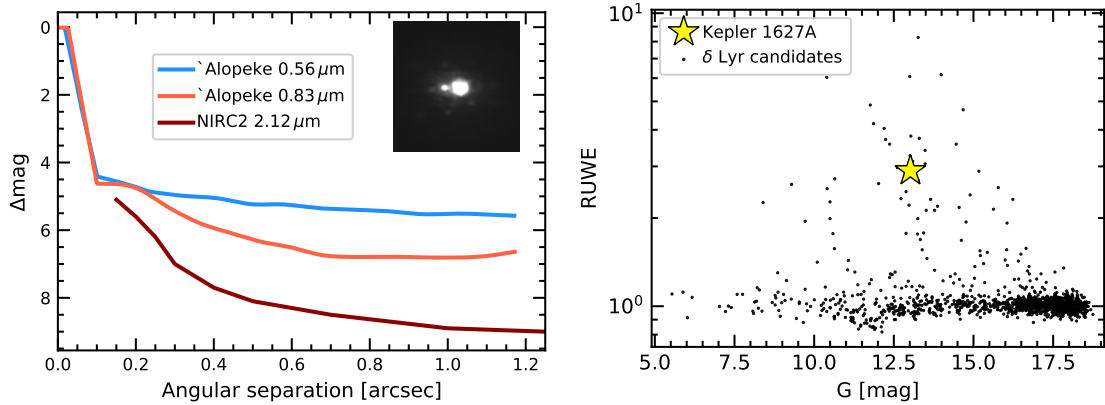


Figure 4. Kepler 1627 is a binary. *Left:* High-resolution imaging from Gemini-North/‘Alopeke and Keck/NIRC2 shows an \approx M2.5V companion at $\rho \approx 0.^{\prime\prime}16$, which corresponds to a projected separation of 53 ± 4 AU. The inset shows a cutout of the stacked NIRC2 image (North is up, East is left, scale is set by the separation of the binary). The lines show $5-\sigma$ contrast limits for the ‘Alopeke filters, and $6-\sigma$ contrast limits for NIRC2 outside of $0.^{\prime\prime}15$. *Right:* Gaia EDR3 renormalized unit weight error (RUWE) point estimates for candidate δ Lyr cluster members. Since other members of the cluster with similar brightnesses have comparable degrees of photometric variability, the high RUWE independently suggests that Kepler 1627 is a binary.

419 0.83 μm and 0.56 μm . We acquired three sets
 420 of 1000×60 msec exposures during good seeing
 421 ($0.45''$), and used the autocorrelation function of
 422 these images to reconstruct a single image and 5-
 423 σ detection limits (see Howell et al. 2011). This
 424 procedure yielded a detection of the companion in
 425 the 0.83 μm notch filter, but not the 0.56 μm filter.
 426 The measured projected separation and magnitude
 427 difference are given in Table 1.

428 Figure 4 summarizes the results of the high-
 429 resolution imaging. The Gaia EDR3 parallax for
 430 the primary implies a projected separation of $53 \pm$
 431 4 AU, assuming the companion is bound. Although
 432 the companion is unresolved in the Gaia source cat-
 433 alog (there are no comoving, codistant candidate
 434 companions brighter than $G < 20.5$ mag within
 435 $\rho < 120''$), its existence was also suggested by the
 436 primary star’s large RUWE relative to other mem-
 437 bers of the δ Lyr cluster (RUWE ≈ 2.9 ; roughly the
 438 98th percentile of the cluster’s distribution). Based
 439 on the apparent separation, the binary orbital pe-
 440 riod is of order hundreds of years. The large
 441 RUWE is therefore more likely to be caused by a
 442 PSF-mismatch skewing the Gaia centroiding dur-
 443 ing successive scans, rather than true astrometric
 444 motion. Regardless, given the low geometric prob-
 445 ability that a companion imaged at $\rho \approx 0.^{\prime\prime}16$ is a
 446 chance line-of-sight companion, we proceed under
 447 the assumption that the companion is bound, and
 448 that Kepler 1627 is a binary. Given the distance
 449 and age, the models of Baraffe et al. (2015) im-
 450 ply a companion mass of $M_B \approx 0.33M_{\odot}$ and com-
 451 panion temperature of $T_{\text{eff},B} \approx 3450$ K. The corre-
 452 sponding spectral type is roughly M2.5V (Pecaut
 453 & Mamajek 2013). These models combined with

454 the NIRC2 contrast limits imply physical limits on
 455 tertiary companions of $M_{\text{ter}} < 50M_{\text{Jup}}$ at $\rho = 50$ AU,
 456 $M_{\text{ter}} < 20M_{\text{Jup}}$ at $\rho = 100$ AU, and $M_{\text{ter}} < 10M_{\text{Jup}}$ at
 457 $\rho = 330$ AU.

4. THE PLANET

4.1. Kepler Light Curve

460 The Kepler space telescope observed Kepler 1627
 461 at a 30-minute cadence from 2009 May 2 until
 462 2013 April 8. Data gaps during quarters 4, 9, and
 463 13 led to an average duty cycle over the 3.9 year
 464 interval of 67%. Kepler 1627 was also observed
 465 at 1-minute cadence from 2012 Oct 5 until 2013
 466 Jan 11. The top panel of Figure 5 shows a por-
 467 tion of the 30-minute cadence PDCSAP light curve.
 468 Nonastrophysical variability has been removed us-
 469 ing the methods discussed by Smith et al. (2017);
 470 the default optimal aperture was assumed (Smith
 471 et al. 2016). Cadences with non-zero quality flags
 472 (9% of the data) have been omitted. The result-
 473 ing photometry is dominated by a quasi-periodic
 474 starspot signal with a peak-to-peak amplitude that
 475 varies between 2% and 8%. Given that the sec-
 476 ondary companion’s brightness in the Kepler band
 477 is $\approx 1.5\%$ that of the primary, source confusion for
 478 the rotation signal is not expected to be an issue.
 479 Previous analyses have identified and characterized
 480 the smaller transit signal (Tenenbaum et al. 2012;
 481 Thompson et al. 2018), validated its planetary na-
 482 ture (Morton et al. 2016), and even searched the
 483 system for transit timing variations (Holczer et al.
 484 2016). Nonetheless, since the cluster membership
 485 provides us with more precise stellar parameters
 486 than those previously available, we opted to reana-
 487 lyze the light curve.

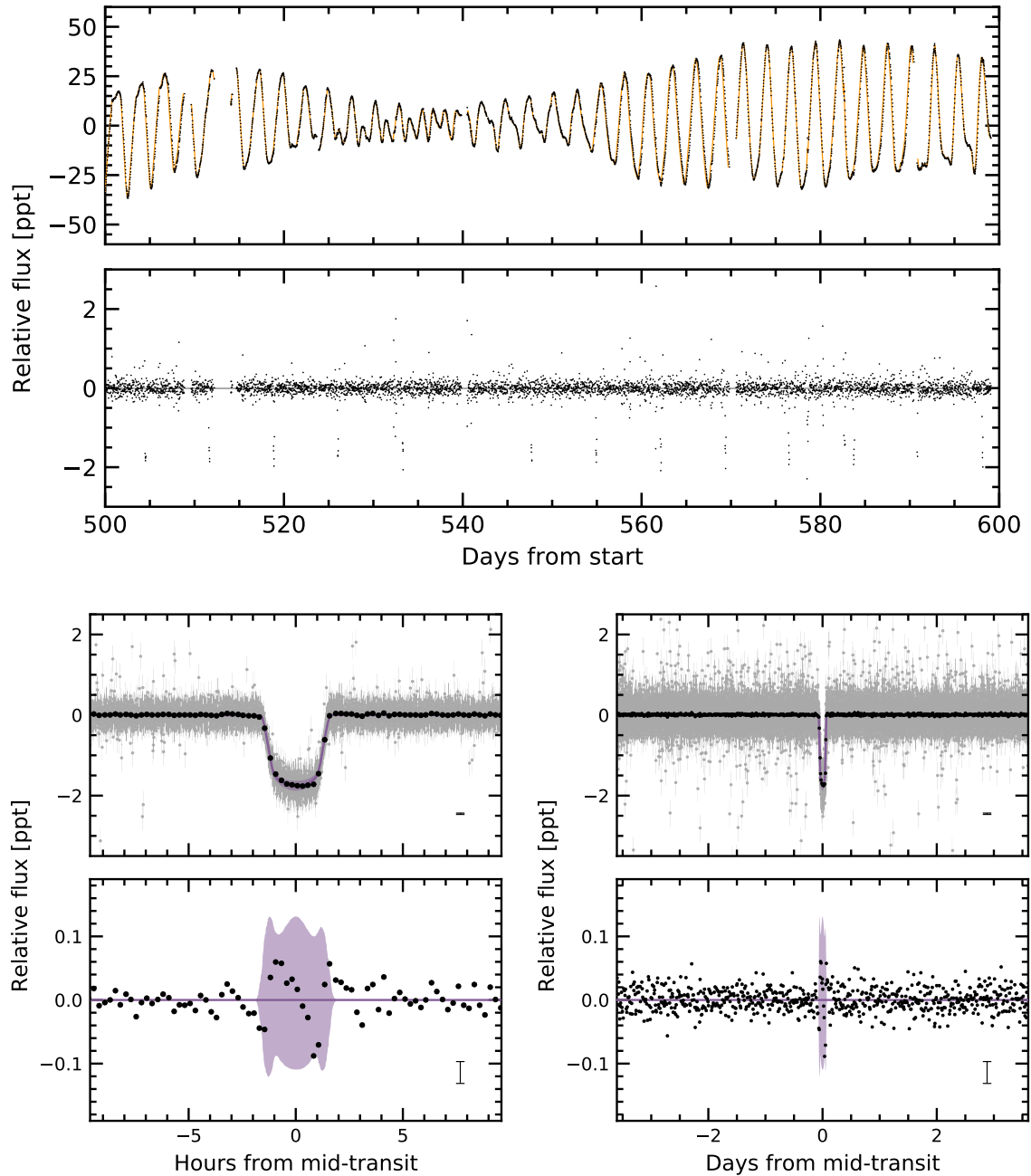


Figure 5. The light curve of Kepler 1627. *Top:* The Kepler data span 1,437 days (3.9 years), sampled at 30 minute cadence; a 100 day segment is shown. The top panel shows the PDCSAP median-subtracted flux in units of parts-per-thousand ($\times 10^{-3}$). The dominant signal is induced by starspots. The stellar variability model (orange line) is subtracted below, revealing the transits of Kepler 1627Ab. The online Figure Set spans the entire 3.9 years of observations. *Bottom:* Phase-folded transit of Kepler 1627Ab with stellar variability removed. Windows over 20 hours (*left*) and the entire orbit (*right*) are shown, and the residual after subtracting the transit is in the bottom-most row. The 2- σ model uncertainties and the best-fit model are the light purple band and the dark purple line. Gray points are individual flux measurements; black points bin these to 15 minute intervals, and have a representative 1- σ error bar in the lower right of each panel. The asymmetric residual during transit is larger than the out-of-transit scatter.

488 **4.1.1. Transit and Stellar Variability Model**

489 We fitted the Kepler long cadence time series with a model that simultaneously included
 490 the planetary transit and the stellar variability. The stellar variability was modeled with
 491 the RotationTerm Gaussian Process kernel in exoplanet (Foreman-Mackey et al. 2020). This
 492 kernel assumes that the variability is generated by
 493 a mixture of two damped simple harmonic oscillators with characteristic frequencies set by $1/P_{\text{rot}}$
 494 and its first harmonic. We additionally included a
 495 jitter term to inflate the flux uncertainties in a manner that accounted for otherwise unmodeled excess
 496 white noise, and let the eccentricity float. For the
 497 limb-darkening, we assumed a quadratic law, and
 498 sampled using the uninformative prior suggested
 499 by Kipping (2013).

500 Our model therefore included 10 free parameters
 501 for the transit ($\{P, t_0, \delta, b, u_1, u_2, R_*, \log g, e, \omega\}$), 2
 502 free parameters for the light curve normalization
 503 and a white noise jitter ($\{\langle f \rangle, \sigma_f\}$), and 5 hyper-
 504 parameters for the GP ($\{\sigma_{\text{rot}}, P_{\text{rot}}, Q_0, dQ, f\}$). We
 505 also considered including an additive SHOTerm
 506 kernel to account for stochastic noise, but found
 507 that this did not affect the results, and so opted for
 508 the simpler GP kernel. We fitted the models using
 509 PyMC3 (Salvatier et al. 2016; Theano Develop-
 510 ment Team 2016), and accounted for the finite
 511 integration time of each exposure in the numerical
 512 integration when evaluating the model light curve
 513 (see Kipping 2010). We assumed a Gaussian like-
 514 lihood, and after initializing each model with the
 515 parameters of the maximum *a posteriori* model,
 516 we sampled using PyMC3’s gradient-based No-U-
 517 Turn Sampler (Hoffman & Gelman 2014) in the
 518 bases indicated in Table 2. We used \hat{R} as our con-
 519 vergence diagnostic (Gelman & Rubin 1992).

520 Figure 5 shows the resulting best-fit model in
 521 orange (top) and purple (bottom). The model
 522 parameters and their uncertainties, given in Ta-
 523 ble 2, are broadly consistent with a Neptune-sized
 524 planet ($3.82 \pm 0.16 R_{\oplus}$) on a close-in circular⁴ or-
 525 bit around a G8V host star ($0.88 \pm 0.02 R_{\odot}$). This
 526 best-fit planet size is consistent with those previ-
 527 ously reported by Morton et al. (2016) and Berger
 528 et al. (2018), and corrects for the small amount of
 529 flux dilution from Kepler 1627B.

535 **4.1.2. Transit Asymmetry**

536 The transit fit however is not perfect: the lower
 537 panels of Figure 5 show an asymmetric residual in
 538 the data relative to the model: the measured flux
 539 is high during the first half of transit, and low in

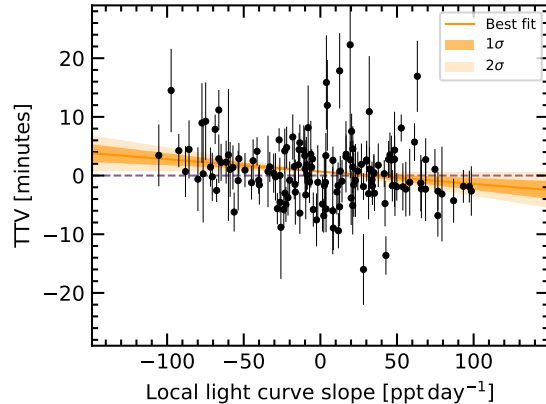


Figure 6. Weak evidence for a prograde orbit of Kepler 1627 Ab. The time of each Kepler transit was measured, along with the local slope of the light curve. The two quantities might be anti-correlated ($\approx 2\sigma$), which could be caused by starspot crossings during the first (second) half of transit inducing a positive (negative) TTV, provided that the orbit is prograde (Mazeh et al. 2015). The units along the abscissa can be understood by considering that the stellar flux changes by ~ 60 ppt per half rotation period (~ 1.3 days).

540 the second half. The semi-amplitude of this devi-
 541 ation is ≈ 50 ppm, which represents a $\approx 3\%$ dis-
 542 tortion of the transit depth ($\delta = 1759 \pm 62$ ppm).
 543 Note that although this asymmetry is within the 2-
 544 σ model uncertainties, the model has a jitter term
 545 that grows to account for excess white noise in the
 546 flux. The significance of the asymmetry is there-
 547 fore best assessed in comparison against the intrin-
 548 sic out-of-transit scatter in the data (≈ 16 ppm), not
 549 the model uncertainties. The lower right panel of
 550 Figure 5 demonstrates that the scatter during transit
 551 is higher than during all other phases of the planet’s
 552 orbit.

553 To determine whether the asymmetry could be a
 554 systematic caused by our stellar variability model,
 555 we explored an alternative approach in which we
 556 isolated each transit window, locally fitted out
 557 polynomial trends, and then binned all the ob-
 558 served transits; the asymmetry was still present at
 559 a comparable amplitude. Appendix B describes a
 560 more detailed analysis, which finds that the asym-
 561 metry also seems to be robust to different meth-
 562 ods of data binning in time and by local light curve
 563 slope. Possible astrophysical explanations are dis-
 564 cussed in Section 5.

565 **4.1.3. Transit Timing and the Local Slope**

566 The previous analysis by Holczer et al. (2016)
 567 did not find any significant long-term transit tim-
 568 ing or duration variations (TTVs or TDVs) for
 569 Kepler 1627. Quantitatively, the mean and stan-
 570 dard deviation of the TTVs and TDVs they mea-

⁴ Our transit fitting yields $e < 0.48$ at 2σ ; the constraints on the eccentricity are not particularly strong.

sured were -1.1 ± 13.8 min and -3.3 ± 22.1 min. In an earlier analysis however, Holczer et al. (2015) studied correlations between TTVs and local light curve slopes, and for Kepler 1627 found a weak correlation of -29 ± 13 min day $^{-1}$ between the two quantities. Given the possible connection between such correlations and the unresolved starspot crossings that we expect to be present in the Kepler 1627 light curve (Mazeh et al. 2015), we opted to re-examine the individual transit times.

We therefore isolated each of the 144 observed transits to within ± 4.5 hr of each transit, and fitted each window with both *i*) a local second or fourth-order polynomial baseline plus the transit, and *ii*) a local linear trend plus the transit. We let the mid-time of each transit float, and then calculated the residual between the measured mid-time and that of a periodic orbit. This residual, the transit timing variation, is plotted in Figure 6 against the local linear slope for the fourth-order polynomial baseline. The slope of -21 ± 10 min day $^{-1}$ is similar to that found by Holczer et al. (2015). The χ^2 of the best-fit line is 306.1, with $n = 140$ data points. An alternative model of a flat line yields $\chi^2 = 315.6$. The difference in the Bayesian information criterion (BIC) between the two models is $BIC_{\text{flat}} - BIC_{\text{line}} = 4.5$, which corresponds to a Bayes factor of ≈ 9.4 . According to the usual Kass & Raftery (1995) criteria, this is “positive” evidence for the model with a finite slope. We view it as suggestive evidence at best, particularly given the excess scatter in the transit timing measurement uncertainties.

A separate concern we had in this analysis was whether our transit fitting procedure might induce spurious correlations between the slope and transit time. In particular, using the second-order polynomial baseline yielded a larger anti-correlation between the TTVs and local slopes, of -79 ± 14 min day $^{-1}$. We therefore performed an injection-recovery procedure in which we injected transits at different phases in the Kepler 1627 light curve and repeated the TTV analysis. This was done at ≈ 50 phases, each separated by $0.02 P_{\text{orb}}$ while omitting the phases in transit. For the second-order polynomial baseline, this procedure yielded a similar anti-correlation in the injected transits as that present in the real transit; using this baseline would therefore bias the result. However for the fourth-order baseline, the correlation present in the data was stronger than in all but one of the injected transits. Possible interpretations are discussed below. Given the lack of statistical significance, this analysis should be interpreted as suggestive at best.

4.2. Planet Confirmation

If the Kepler 1627Ab transit signal is created by a genuine planet, then to our knowledge it would

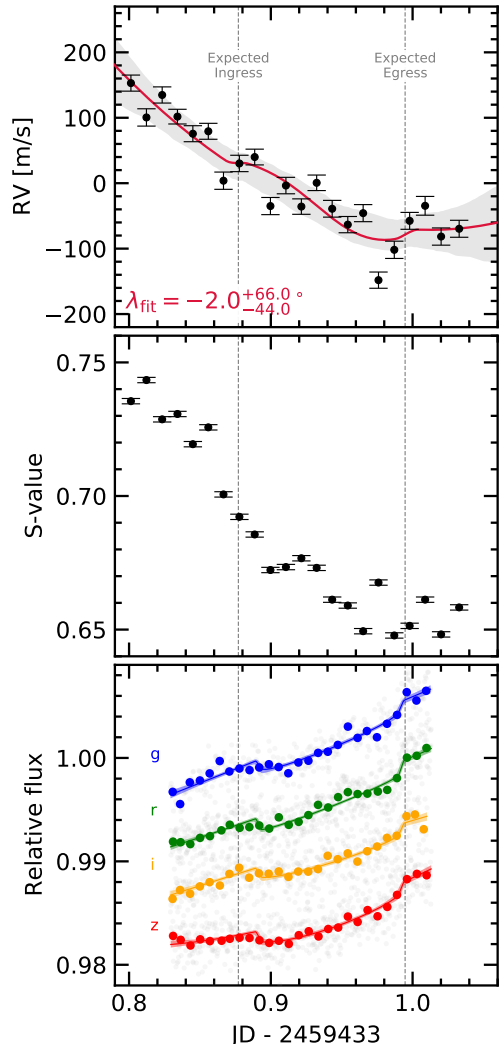


Figure 7. Keck/HIRES radial velocities and MuSCAT3 photometry from the transit of 2021 Aug 7. *Top:* The radial velocity jitter across the 15 minute exposures ($\sigma_{\text{RV}} \approx 30 \text{ m s}^{-1}$) prevented us from detecting the RM effect; a model including the RM anomaly and a quadratic trend in time to fit the spot-induced $\approx 250 \text{ m s}^{-1}$ trend is shown (see Appendix C). Shaded bands show $2-\sigma$ model uncertainties. *Middle:* The RV variations are strongly correlated with varying emission in the Ca H and K lines. *Bottom:* The photometric transit depths are consistent across the *griz* bandpasses. The photometry is binned at 10 minute intervals.

be the youngest planet yet found by the prime Kepler mission.⁵ Could the transit be produced by anything other than a planet orbiting this near-

⁵ The re-purposed K2 mission however has found two younger systems containing five planets: K2-33b (9 ± 1 Myr; Mann et al. 2016; David et al. 2016) and V1298 Tau (23 ± 4 Myr; David et al. 2019).

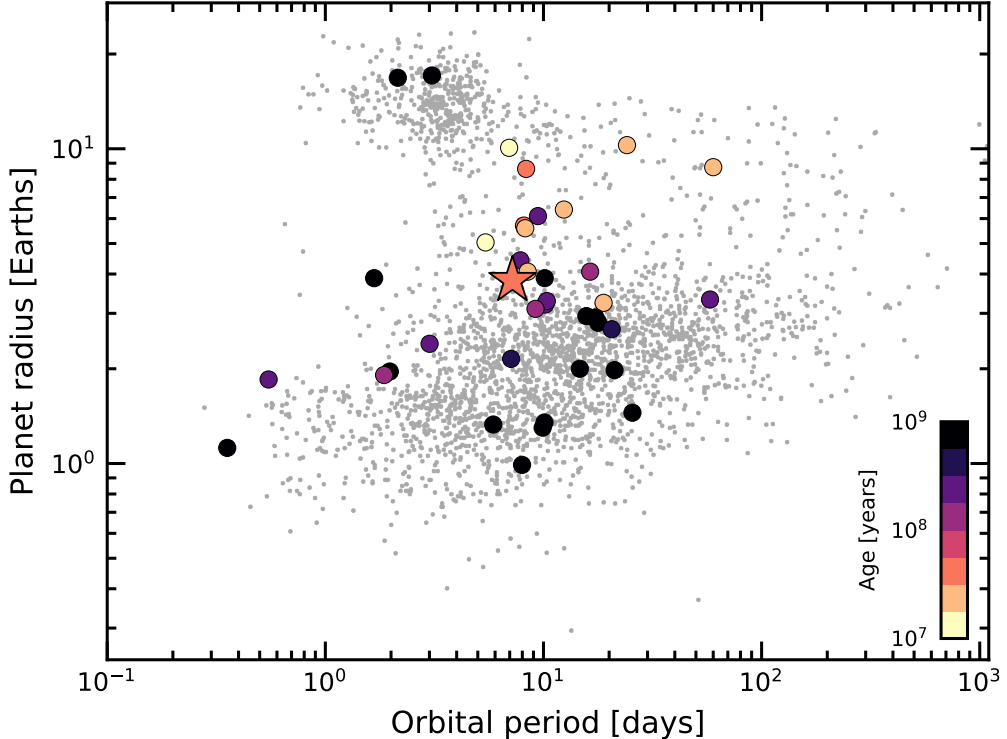


Figure 8. Radii, orbital periods, and ages of transiting exoplanets. Planets younger than a gigayear with $\tau/\sigma_\tau > 3$ are emphasized, where τ is the age and σ_τ is its uncertainty. Kepler 1627Ab is shown with a star. The large sizes of the youngest transiting planets could be explained by their primordial atmospheres not yet having evaporated; direct measurements of the atmospheric outflows or planetary masses would help to confirm this expectation. Selection effects may also be important. Parameters are from the NASA Exoplanet Archive (2021 Sept 15).

solar analog? Morton et al. (2016) validated the planet based on the transit shape, arguing that the most probable false positive scenario was that of a background eclipsing binary, which had a model-dependent probability of $\approx 10^{-5}$. However, this calculation was performed without knowledge of the low-mass stellar companion ($M_B \approx 0.33 M_\odot$). Validated planets have also previously been refuted (e.g., Shporer et al. 2017). We therefore reassessed false positive scenarios in some detail.

As an initial plausibility check, Kepler 1627B contributes 1% to 2% of the total flux observed in the Kepler aperture. For the sake of argument, assume the former value. The observed transit has a depth of $\approx 0.18\%$. A 18% deep eclipse of Kepler 1627B would therefore be needed to produce a signal with the appropriate depth. The shape of the transit signal however requires the impact parameter to be below 0.77 (2- σ); the tertiary transiting the secondary would therefore need to be non-grazing with $R_3/R_2 \approx 0.4$. This yields a contradiction: this scenario requires an ingress and egress phase that each span $\approx 40\%$ of the transit duration (≈ 68 min). The actual measured ingress and egress duration is ≈ 17 min, a factor of four times too short. The combination of Kepler 1627B's

brightness, the transit depth, and the ingress duration therefore disfavor the scenario that Kepler 1627B might host the transit signal.

Beyond this simple test, a line of evidence that effectively confirms the planetary interpretation is that the stellar density implied by the transit duration and orbital period is inconsistent with an eclipsing body around the M-dwarf companion. We find $\rho_* = 2.00 \pm 0.24 \text{ g cm}^{-3}$, while the theoretically expected density for Kepler 1627B is $\approx 4.6 \text{ g cm}^{-3}$ (Baraffe et al. 2015). The transit duration is therefore too long to be explained by a star eclipsing the M dwarf secondary at $10-\sigma$. While the planet might hypothetically still orbit a hidden close and bright companion, this possibility is implausible given *i*) the lack of secondary lines in the HIRES spectra, *ii*) the lack of secondary rotation signals in the Kepler photometry, and *iii*) the proximity of Kepler 1627 to the δ Lyr cluster locus on the Gaia CAMD (Figure 3).

The correlation noted in Section 4.1.3 between the TTVs and the local light curve slope might be an additional line of evidence in support of the planetary interpretation. Unless it is a statistical fluke (a $\approx 5\%$ possibility), then the most likely cause of the correlation is unresolved starspot

crossings (Mazeh et al. 2015). These would only be possible if the planet transits the primary star, which excludes a background eclipsing binary scenario. The correlation would also suggest that the planet’s orbit is prograde. The latter point assumes that the dominant photometric variability is induced by dark spots, and not bright faculae. Given the observed transition of Sun-like stellar variability from spot to faculae-dominated regimes between young and old ages, we expect this latter assumption to be reasonably secure (Shapiro et al. 2016; Montet et al. 2017; Reinhold & Hekker 2020).

A third supporting line of evidence for the planetary interpretation also exists. We observed a transit of Kepler 1627Ab on the night of 2021 Aug 7 spectroscopically with HIRES at the Keck-I telescope and photometrically in *griz* bands with MuSCAT3 at Haleakalā Observatory. Details of the observation sequence are discussed in Appendix C; Figure 7 shows the results. Although we did not detect the Rossiter-McLaughlin (RM) anomaly, the multi-band MuSCAT3 light curves show that the transit is achromatic. Quantitatively, when we fitted the MuSCAT3 photometry with a model that lets the transit depths vary across each bandpass, we found *griz* depths consistent with the Kepler depth at 0.6, 0.3, 0.3, and 1.1σ respectively. The achromatic transits strongly favor Kepler 1627A as the transit host, since Kepler 1627B is a much redder star. Conditioned on the ephemeris and transit depth from the Kepler data, the MuSCAT3 observations also suggested a transit duration 17.3 ± 4.3 min shorter than the Kepler transits. However, given both the lack of TDVs in the Kepler data and the relatively low signal-to-noise of the MuSCAT3 transit, further photometric follow-up would be necessary to determine whether the transit duration is actually changing.

For our RM analysis, the details are discussed in Appendix C. While the velocities are marginally more consistent with a prograde or polar orbit than a retrograde orbit, the spot-corrected exposure-to-exposure scatter ($\sigma_{RV} \approx 30 \text{ m s}^{-1}$) is comparable to the expected RM anomaly assuming an aligned orbit ($\Delta v_{RM} \approx 20 \text{ m s}^{-1}$). We are therefore not in a position to claim a spectroscopic detection of the RM effect, nor to quantify the stellar obliquity.

5. DISCUSSION & CONCLUSIONS

Kepler 1627Ab provides a new extremum in the ages of the Kepler planets, and opens multiple avenues for further study. Observations of spectroscopic transits at greater signal-to-noise should yield a measurement of the stellar obliquity, which would confirm or refute the prograde orbital geometry suggested by the TTV-local slope correlation. Separately, transit spectroscopy aimed at

detecting atmospheric outflows could yield insight into the evolutionary state of the atmosphere (e.g., Ehrenreich et al. 2015; Spake et al. 2018; Vissapragada et al. 2020). Observations that quantify the amount of high-energy irradiation incident on the planet would complement these efforts, by helping to clarify the expected outflow rate (e.g., Poppenhaeger et al. 2021). Finally, a challenging but informative quantity to measure would be the planet’s mass. Measured at sufficient precision, for instance through a multi-wavelength radial velocity campaign, the combination of the size, mass, and age would yield constraints on both the planet’s composition and its initial entropy (Owen 2020).

More immediately, the Kepler data may yet contain additional information. For instance, one possible explanation for the transit asymmetry shown in Figure 5 is that of a dusty asymmetric outflow. Dusty outflows are theoretically expected for young mini-Neptunes, and the amplitude of the observed asymmetry is consistent with predictions (Wang & Dai 2019). A second possibility is that the planetary orbit is slightly misaligned from the stellar spin axis, and tends to transit starspot groups at favored stellar latitudes. This geometry would be necessary in order to explain how the starspot crossings could add up coherently, given that the planetary orbital period (7.203 days) and the stellar rotation period (2.642 days) are not a rational combination. Other possibilities including gravity darkening or TTVs causing the asymmetry are disfavored (see Appendix B).

Beyond the asymmetric transits, Appendix D highlights an additional abnormality in the short-cadence Kepler data, in the arrival time distribution of stellar flares. We encourage its exploration by investigators more versed in the topic than ourselves.

In the context of the transiting planet population, Kepler 1627Ab is among the youngest known (Figure 8). Comparable systems with precise ages include K2-33 (Mann et al. 2016; David et al. 2016), DS Tuc (Benatti et al. 2019; Newton et al. 2019), HIP 67522 (Rizzuto et al. 2020), TOI 837 (Bouma et al. 2020), the two-planet AU Mic (Plavchan et al. 2020; Martioli et al. 2021) and the four-planet V1298 Tau (David et al. 2019). Kepler 1627Ab is one of the smaller planets in this sample ($3.82 \pm 0.16 R_\oplus$), which could be linked to the selection effects imposed by spot-induced photometric variability at very young ages (e.g., Zhou et al. 2021). However, it seems that smaller planets could have been detected: based on the per-target detection contours, the Kepler pipeline’s median completeness extended to $1.6 R_\oplus$ at 10 day orbital periods, and $3.3 R_\oplus$ at 100 days (Burke & Catanzarite 2021). These limits account for the spot-

induced variability in the system through a correction based on the Combined Differential Photometric Precision (CDPP) in the Kepler 1627 light curve over the relevant transit timescales (Burke & Catanzarite 2017). The large size of Kepler 1627Ab relative to most Kepler mini-Neptunes might therefore support a picture in which the typical $5 M_{\oplus}$ mini-Neptune (Wu 2019) loses a significant fraction of its primordial atmosphere over its first gigayear (Owen & Wu 2013; Ginsburg et al. 2018). It could also be consistent with a scenario in which an earlier “boil-off” of the planet’s atmosphere during disk dispersal decreases the entropy of the planetary interior, leading to a $\sim 10^8$ year Kelvin-Helmholtz cooling and contraction timescale (Owen 2020). Confirming either of these scenarios would require a measurement of the planetary mass; otherwise, alternative explanations for its large size also include that it is abnormally massive, or that it has an abnormally large envelope to core mass ratio.

Ultimately, the main advance of this work is a precise measurement of the age of Kepler 1627Ab. This measurement was enabled by identifying the connection of the star to the δ Lyr cluster using Gaia kinematics, and by then using the Gaia color-absolute magnitude diagram and TESS stellar rotation periods to verify the cluster’s existence. Table 3 enables similar cross-matches for both known and forthcoming exoplanet systems (e.g., Guerrero et al. 2021). Confirming these candidate associations using independent age indicators is essential because their false positive rates are not known. A related path is to identify new kinematic associations around known exoplanet host stars using positions and tangential velocities from Gaia, and to verify these associations with stellar rotation periods and spectroscopy (e.g., Tofflemire et al. 2021). Each approach seems likely to expand the census of planets with precisely measured ages over the coming years, which will help in deciphering the early stages of exoplanet evolution.

ACKNOWLEDGMENTS

The authors are grateful to J. Winn, J. Spake, A. Howard, and T. David for illuminating discussions and suggestions, and to R. Kerr for providing us with the Kerr et al. (2021) membership list prior to its publication. The authors are also grateful to K. Collins for helping resolve the scheduling conflict that would have otherwise prevented the MuSCAT3 observations. L.G.B. acknowledges support from a Charlotte Elizabeth Procter Fellowship from Princeton University, as well as from the TESS GI Program (NASA grants

80NSSC19K0386 and 80NSSC19K1728) and the Heising-Simons Foundation (51 Pegasi b Fellowship). Keck/NIRC2 imaging was acquired by program 2015A/N301N2L (PI: A. Kraus). In addition, this paper is based in part on observations made with the MuSCAT3 instrument, developed by the Astrobiology Center and under financial support by JSPS KAKENHI (JP18H05439) and JST PRESTO (JPMJPR1775), at Faulkes Telescope North on Maui, HI, operated by the Las Cumbres Observatory. This work is partly supported by JSPS KAKENHI Grant Numbers 22000005, JP15H02063, JP17H04574, JP18H05439, JP18H05442, JST PRESTO Grant Number JPMJPR1775, the Astrobiology Center of National Institutes of Natural Sciences (NINS) (Grant Number AB031010). This paper also includes data collected by the TESS mission, which are publicly available from the Mikulski Archive for Space Telescopes (MAST). Funding for the TESS mission is provided by NASA’s Science Mission directorate. We thank the TESS Architects (G. Ricker, R. Vanderspek, D. Latham, S. Seager, J. Jenkins) and the many TESS team members for their efforts to make the mission a continued success. Finally, this research has made use of the Keck Observatory Archive (KOA), which is operated by the W. M. Keck Observatory and the NASA Exoplanet Science Institute (NExScI), under contract with the National Aeronautics and Space Administration. We also thank the Keck Observatory staff for their support of HIRES and remote observing. We recognize the importance that the summit of Maunakea has within the indigenous Hawaiian community, and are deeply grateful to have the opportunity to conduct observations from this mountain.

Software: `altaipony` (Ilin et al. 2021), `astrobase` (Bhatti et al. 2018), `astropy` (Astropy Collaboration et al. 2018), `astroquery` (Ginsburg et al. 2018), `corner` (Foreman-Mackey 2016), `exoplanet` (Foreman-Mackey et al. 2020), and its dependencies (Agol et al. 2020; Kipping 2013; Luger et al. 2019; Theano Development Team 2016), `PyMC3` (Salvatier et al. 2016), `scipy` (Jones et al. 2001), `TESS-point` (Burke et al. 2020), `wotan` (Hippke et al. 2019).

Facilities: *Astrometry:* Gaia (Gaia Collaboration et al. 2018b, 2021a). *Imaging:* Second Generation Digitized Sky Survey. Keck:II (NIRC2; www2.keck.hawaii.edu/inst/nirc2). Gemini:North (‘Alopeke; Scott et al. 2018, 2021). *Spectroscopy:* Keck:I (HIRES; Vogt et al. 1994). *Photometry:* Kepler (Borucki et al. 2010), MuSCAT3 (Narita et al. 2020), TESS (Ricker et al. 2015).

Table 1. Literature and Measured Properties for Kepler 1627

Primary Star			
TIC 120105470 GAIADR2 [†] 2103737241426734336			
Parameter	Description	Value	Source
$\alpha_{J2015.5}$	Right Ascension (hh:mm:ss)	18:56:13.6	1
$\delta_{J2015.5}$	Declination (dd:mm:ss)	+41:34:36.22	1
V	Johnson V mag.	13.11 \pm 0.08	2
G	Gaia G mag.	13.02 \pm 0.02	1
G_{BP}	Gaia BP mag.	13.43 \pm 0.02	1
G_{RP}	Gaia RP mag.	12.44 \pm 0.02	1
T	TESS T mag.	12.53 \pm 0.02	2
J	2MASS J mag.	11.69 \pm 0.02	3
H	2MASS H mag.	11.30 \pm 0.02	3
K _S	2MASS K _S mag.	11.19 \pm 0.02	3
π	Gaia EDR3 parallax (mas)	3.009 \pm 0.032	1
d	Distance (pc)	329.5 \pm 3.5	1, 4
μ_α	Gaia EDR3 proper motion	1.716 \pm 0.034	1
	in RA (mas yr ⁻¹)		
μ_δ	Gaia EDR3 proper motion	-1.315 \pm 0.034	1
	in DEC (mas yr ⁻¹)		
RUWE	Gaia EDR3 renormalized	2.899	1
	unit weight error		
RV	Systemic radial velocity (km s ⁻¹)	-16.7 \pm 1.0	5
Spec. Type	Spectral Type	G8V	5
$v \sin i_*$	Rotational velocity* (km s ⁻¹)	18.9 \pm 1.0	5
Li EW	6708Å Equiv. Width (mÅ)	235 ⁺⁵ ₋₇	5
T_{eff}	Effective Temperature (K)	5505 \pm 60	6
$\log g_*$	Surface Gravity (cgs)	4.53 \pm 0.05	6
R_*	Stellar radius (R_\odot)	0.881 \pm 0.018	6
M_*	Stellar mass (R_\odot)	0.953 \pm 0.019	6
Av	Interstellar reddening (mag)	0.2 \pm 0.1	6
[Fe/H]	Metallicity	0.1 \pm 0.1	6
P_{rot}	Rotation period (d)	2.642 \pm 0.042	7
Age	Adopted stellar age (Myr)	38 ⁺⁶ ₋₅	8
Δm_{832}	Mag difference ('Alopeke 832 nm)	3.14 \pm 0.15	9
θ_B	Position angle (deg)	92 \pm 1	9
ρ_B	Apparent separation of	0.164 \pm 0.002	9
	primary and secondary (as)		
ρ_B	Apparent separation of	53 \pm 4	1, 4, 9
	primary and secondary (AU)		
$\Delta m_{K'}$	Mag difference (NIRC2 K')	2.37 \pm 0.02	10
θ_B	Position angle (deg)	95.9 \pm 0.5	10
ρ_B	Apparent separation of	0.1739 \pm 0.0010	10
	primary and secondary (as)		

NOTE—[†] The GAIADR2 and GAIAEDR3 identifiers for Kepler 1627A are identical. The secondary is not resolved in the Gaia point source catalog. * Given only $v \sin i$ and $2\pi R_*/P_{\text{rot}}$, $\cos i = 0.11^{+0.11}_{-0.08}$. Provenances are: ¹Gaia Collaboration et al. (2021a), ²Stassun et al. (2019), ³Skrutskie et al. (2006), ⁴Lindgren et al. (2021), ⁵HIRESS spectra and Yee et al. (2017), ⁶Cluster isochrone (MIST adopted; PARSEC compared for quoted uncertainty), ⁷Kepler light curve, ⁸Pre-main-sequence CAMD interpolation (Section 2.2.1), ⁹'Alopeke imaging 2021 June 24 (Scott et al. 2021), ¹⁰NIRC2 imaging 2015 July 22, using the Yelda et al. (2010) optical distortion solution to convert pixel-space relative positions to on-sky relative astrometry. The “discrepancy” between the two imaging epochs likely indicates orbital motion.

Table 2. Priors and Posteriors for Model Fitted to the Long Cadence Kepler 1627Ab Light Curve.

Param.	Unit	Prior	Median	Mean	Std. Dev.	3%	97%	ESS	$\hat{R} - 1$
<i>Sampled</i>									
P	d	$\mathcal{N}(7.20281; 0.01000)$	7.2028038	7.2028038	0.0000073	7.2027895	7.2028168	7464	3.9e-04
$t_0^{(1)}$	d	$\mathcal{N}(120.79053; 0.02000)$	120.7904317	120.7904254	0.0009570	120.7886377	120.7921911	3880	2.0e-03
$\log \delta$	—	$\mathcal{N}(-6.3200; 2.0000)$	-6.3430	-6.3434	0.0354	-6.4094	-6.2767	6457	3.0e-04
$b^{(2)}$	—	$\mathcal{U}(0.000; 1.000)$	0.4669	0.4442	0.2025	0.0662	0.8133	1154	1.6e-03
u_1	—	Kipping (2013)	0.271	0.294	0.190	0.000	0.628	3604	1.5e-03
u_2	—	Kipping (2013)	0.414	0.377	0.326	-0.240	0.902	3209	1.4e-03
R_*	R_{\odot}	$\mathcal{N}(0.881; 0.018)$	0.881	0.881	0.018	0.847	0.915	8977	3.1e-04
$\log g$	cgs	$\mathcal{N}(4.530; 0.050)$	4.532	4.533	0.051	4.435	4.627	6844	1.6e-03
$\langle f \rangle$	—	$\mathcal{N}(0.000; 0.100)$	-0.0003	-0.0003	0.0001	-0.0005	-0.0000	8328	1.1e-03
$e^{(3)}$	—	Van Eylen et al. (2019)	0.154	0.186	0.152	0.000	0.459	1867	2.0e-03
ω	rad	$\mathcal{U}(0.000; 6.283)$	0.055	0.029	1.845	-3.139	2.850	3557	8.6e-05
$\log \sigma_f$	—	$\mathcal{N}(\log \langle \sigma_f \rangle; 2.000)$	-8.035	-8.035	0.008	-8.049	-8.021	9590	3.9e-04
σ_{rot}	d^{-1}	InvGamma(1.000; 5.000)	0.070	0.070	0.001	0.068	0.072	9419	1.4e-03
$\log P_{\text{rot}}$	log(d)	$\mathcal{N}(0.958; 0.020)$	0.978	0.978	0.001	0.975	0.980	8320	2.2e-04
$\log Q_0$	—	$\mathcal{N}(0.000; 2.000)$	-0.327	-0.326	0.043	-0.407	-0.246	9659	2.7e-04
$\log dQ$	—	$\mathcal{N}(0.000; 2.000)$	7.697	7.698	0.103	7.511	7.899	5824	3.7e-04
f	—	$\mathcal{U}(0.010; 1.000)$	0.01006	0.01009	0.00009	0.01000	0.01025	4645	4.0e-04
<i>Derived</i>									
δ	—	—	0.001759	0.001759	0.000062	0.001641	0.001875	6457	3.0e-04
R_p/R_*	—	—	0.039	0.039	0.001	0.037	0.042	1811	1.1e-03
ρ_*	g cm^{-3}	—	1.990	2.004	0.240	1.570	2.461	6905	2.1e-03
$R_p^{(4)}$	R_{Jup}	—	0.337	0.338	0.014	0.314	0.367	2311	1.0e-03
$R_p^{(4)}$	R_{Earth}	—	3.777	3.789	0.157	3.52	4.114	2311	1.0e-03
a/R_*	—	—	17.606	17.619	0.702	16.277	18.906	6905	2.1e-03
$\cos i$	—	—	0.027	0.025	0.010	0.004	0.040	1312	1.2e-03
T_{14}	hr	—	2.841	2.843	0.060	2.734	2.958	3199	3.6e-04
T_{13}	hr	—	2.555	2.539	0.094	2.360	2.692	1960	1.4e-03

NOTE— ESS refers to the number of effective samples. \hat{R} is the Gelman-Rubin convergence diagnostic. Logarithms in this table are base-e. \mathcal{U} denotes a uniform distribution, and \mathcal{N} a normal distribution. (1) The ephemeris is in units of BJDTDB - 2454833. (2) Although $\mathcal{U}(0, 1 + R_p/R_*)$ is formally correct, for this model we assumed a non-grazing transit to enable sampling in $\log \delta$. (3) The eccentricity vectors are sampled in the $(e \cos \omega, e \sin \omega)$ plane. (4) The true planet size is a factor of $((F_1 + F_2)/F_1)^{1/2}$ larger than that from the fit because of dilution from Kepler 1627B, where F_1 is the flux from the primary, and F_2 is that from the secondary; the mean and standard deviation of $R_p = 3.817 \pm 0.158 R_{\oplus}$ quoted in the text includes this correction, assuming $(F_1 + F_2)/F_1 \approx 1.015$.

Table 3. Young, Age-dated, and Age-dateable Stars Within the Nearest Few Kiloparsecs.

Parameter	Example Value	Description
source_id	1709456705329541504	Gaia DR2 source identifier.
ra	247.826	Gaia DR2 right ascension [deg].
dec	79.789	Gaia DR2 declination [deg].
parallax	35.345	Gaia DR2 parallax [mas].
parallax_error	0.028	Gaia DR2 parallax uncertainty [mas].
pmra	94.884	Gaia DR2 proper motion $\mu_{\alpha} \cos \delta$ [mas yr $^{-1}$].
pmdec	-86.971	Gaia DR2 proper motion μ_{δ} [mas yr $^{-1}$].
phot_g_mean_mag	6.85	Gaia DR2 G magnitude.
phot_bp_mean_mag	6.409	Gaia DR2 G_{BP} magnitude.
phot_rp_mean_mag	7.189	Gaia DR2 G_{RP} magnitude.
cluster	NASAExoArchive_ps_20210506.Uma,IR_excess	Comma-separated cluster or group name.
age	9.48,nan,nan	Comma-separated logarithm (base-10) of reported ^a age in years.
mean_age	9.48	Mean (ignoring NaNs) of age column.
reference_id	NASAExoArchive_ps_20210506,Ujjwal2020,CottenSong2016	Comma-separated provenance of group membership.
reference_bibcode	2013PASP..125..989A,2020AJ....159..166U,2016ApJS..225..15C	ADS bibcode corresponding to reference_id.

NOTE— Table 3 is published in its entirety in a machine-readable format. This table is a concatenation of the studies listed in Table 4. One entry is shown for guidance regarding form and content. In this particular example, the star has a cold Jupiter on a 16 year orbit, HD 150706b (Boisse et al. 2012). An infrared excess has been reported (Cotten & Song 2016), and the star was identified by Ujjwal et al. (2020) as a candidate UMa moving group member (≈ 400 Myr; Mann et al. 2020). The star's RV activity and TESS rotation period corroborate its youth.

Table 4. Provenances of Young and Age-dateable Stars.

Reference	N_{Gaia}	N_{Age}	$N_{G_{\text{RP}} < 16}$
Kounkel et al. (2020)	987376	987376	775363
Cantat-Gaudin & Anders (2020)	433669	412671	269566
Cantat-Gaudin et al. (2018)	399654	381837	246067
Kounkel & Covey (2019)	288370	288370	229506
Cantat-Gaudin et al. (2020)	233369	227370	183974
Zari et al. (2018) UMS	86102	0	86102
Wenger et al. (2000) Y*?	61432	0	45076
Zari et al. (2018) PMS	43719	0	38435
Gaia Collaboration et al. (2018a) $d > 250 \text{ pc}$	35506	31182	18830
Castro-Ginard et al. (2020)	33635	24834	31662
Kerr et al. (2021)	30518	25324	27307
Wenger et al. (2000) Y*○	28406	0	16205
Villa Vélez et al. (2018)	14459	14459	13866
Cantat-Gaudin et al. (2019)	11843	11843	9246
Damiani et al. (2019) PMS	10839	10839	9901
Oh et al. (2017)	10379	0	10370
Meingast et al. (2021)	7925	7925	5878
Wenger et al. (2000) pMS*	5901	0	3006
Gaia Collaboration et al. (2018a) $d < 250 \text{ pc}$	5378	817	3968
Kounkel et al. (2018)	5207	3740	5207
Ratzenböck et al. (2020)	4269	4269	2662
Wenger et al. (2000) TT*	4022	0	3344
Damiani et al. (2019) UMS	3598	3598	3598
Rizzuto et al. (2017)	3294	3294	2757
Akeson et al. (2013)	3107	868	3098
Tian (2020)	1989	1989	1394
Goldman et al. (2018)	1844	1844	1783
Cotten & Song (2016)	1695	0	1693
Gagné et al. (2018b)	1429	0	1389
Röser & Schilbach (2020) Psc-Eri	1387	1387	1107
Röser & Schilbach (2020) Pleiades	1245	1245	1019
Wenger et al. (2000) TT?	1198	0	853
Gagné & Faherty (2018)	914	0	913
Pavlidou et al. (2021)	913	913	504
Gagné et al. (2018a)	692	0	692
Ujjwal et al. (2020)	563	0	563
Gagné et al. (2020)	566	566	351
Esplin & Luhman (2019)	377	443	296
Roccatagliata et al. (2020)	283	283	232
Meingast & Alves (2019)	238	238	238
Fürnkranz et al. (2019) Coma-Ber	214	214	213
Fürnkranz et al. (2019) Neighbor Group	177	177	167
Kraus et al. (2014)	145	145	145

NOTE— Table 4 describes the provenances for the young and age-dateable stars in Table 3. N_{Gaia} : number of Gaia stars we parsed from the literature source. N_{Age} : number of stars in the literature source with ages reported. $N_{G_{\text{RP}} < 16}$: number of Gaia stars we parsed from the literature source with either $G_{\text{RP}} < 16$, or a parallax S/N exceeding 5 and a distance closer than 100 pc. The latter criterion included a few hundred white dwarfs that would have otherwise been neglected. Some studies are listed multiple times if they contain multiple tables. Wenger et al. (2000) refers to the SIMBAD database.

REFERENCES

- 905 Agol, E., Luger, R., & Foreman-Mackey, D. 2020, *AJ*,
 906 159, 123
- 907 Akeson, R. L., Chen, X., Ciardi, D., et al. 2013, *PASP*,
 908 125, 989
- 909 Astropy Collaboration, Price-Whelan, A. M., Sipőcz,
 910 B. M., et al. 2018, *AJ*, 156, 123
- 911 Baraffe, I., Homeier, D., Allard, F., & Chabrier, G.
 912 2015, *A&A*, 577, A42
- 913 Beaumont, C., Robitaille, T., Borkin, M., & Goodman,
 914 A. 2014, glueviz v0.4: multidimensional data
 915 exploration
- 916 Benatti, S., Nardiello, D., Malavolta, L., et al. 2019,
 917 *A&A*, 630, A81
- 918 Berger, T. A., Howard, A. W., & Boesgaard, A. M.
 919 2018, *ApJ*, 855, 115
- 920 Berger, T. A., Huber, D., Gaidos, E., & van Saders, J. L.
 921 2018, *ApJ*, 866, 99
- 922 Bhatti, W., Bouma, L. G., & Wallace, J. 2018,
 923 astrobase,
 924 <https://doi.org/10.5281/zenodo.1469822>
- 925 Boisse, I., Pepe, F., Perrier, C., et al. 2012, *A&A*, 545,
 926 A55
- 927 Borucki, W. J., Koch, D., Basri, G., et al. 2010, *Science*,
 928 327, 977
- 929 Bossini, D., Vallenari, A., Bragaglia, A., et al. 2019,
 930 *A&A*, 623, A108
- 931 Bouma, L. G., Curtis, J. L., Hartman, J. D., Winn, J. N.,
 932 & Bakos, G. A. 2021, arXiv:2107.08050 [astro-ph]
- 933 Bouma, L. G., Hartman, J. D., Bhatti, W., Winn, J. N.,
 934 & Bakos, G. Á. 2019, *ApJS*, 245, 13
- 935 Bouma, L. G., Hartman, J. D., Brahm, R., et al. 2020,
 936 *AJ*, 160, 239
- 937 Bressan, A., Marigo, P., Girardi, L., et al. 2012,
 938 *MNRAS*, 427, 127
- 939 Burke, C., & Catanzarite, J. 2021, KeplerPORTS:
 940 Kepler Planet Occurrence Rate Tools
- 941 Burke, C. J., & Catanzarite, J. 2017, Planet Detection
 942 Metrics: Per-Target Detection Contours for Data
 943 Release 25, Kepler Science Document
 944 KSCI-19111-002
- 945 Burke, C. J., Levine, A., Fausnaugh, M., et al. 2020,
 946 TESS-Point: High precision TESS pointing tool,
 947 Astrophysics Source Code Library, ascl:2003.001
- 948 Cantat-Gaudin, T., & Anders, F. 2020, *A&A*, 633, A99
- 949 Cantat-Gaudin, T., Jordi, C., Vallenari, A., et al. 2018,
 950 *A&A*, 618, A93
- 951 Cantat-Gaudin, T., Jordi, C., Wright, N. J., et al. 2019,
 952 *A&A*, 626, A17
- 953 Cantat-Gaudin, T., Anders, F., Castro-Ginard, A., et al.
 954 2020, *A&A*, 640, A1
- 955 Capitanio, L., Lallement, R., Vergely, J. L., Elyajouri,
 956 M., & Monreal-Ibero, A. 2017, *A&A*, 606, A65
- 957 Castro-Ginard, A., Jordi, C., Luri, X., et al. 2020, *A&A*,
 958 635, A45
- 959 Choi, J., Dotter, A., Conroy, C., et al. 2016, *ApJ*, 823,
 960 102
- 961 Claret, A., & Bloemen, S. 2011, *A&A*, 529, A75
- 962 Cotten, T. H., & Song, I. 2016, *ApJS*, 225, 15
- 963 Dahm, S. E. 2015, *ApJ*, 813, 108
- 964 Dai, F., Winn, J. N., Berta-Thompson, Z.,
 965 Sanchis-Ojeda, R., & Albrecht, S. 2018, *AJ*, 155, 177
- 966 Damiani, F., Prisinzano, L., Pillitteri, I., Micela, G., &
 967 Sciotino, S. 2019, *A&A*, 623, A112
- 968 Davenport, J. R. A. 2016, *ApJ*, 829, 23
- 969 Davenport, J. R. A., Hawley, S. L., Hebb, L., et al.
 970 2014, *ApJ*, 797, 122
- 971 David, T., Hillenbrand, L., & Petigura, E. 2016, *Nature*,
 972 534, 658
- 973 David, T. J., & Hillenbrand, L. A. 2015, *ApJ*, 804, 146
- 974 David, T. J., Petigura, E. A., Luger, R., et al. 2019,
 975 *ApJL*, 885, L12
- 976 David, T. J., Contardo, G., Sandoval, A., et al. 2021, *AJ*,
 977 161, 265
- 978 Dias, W. S., Monteiro, H., Caetano, T. C., et al. 2014,
 979 *A&A*, 564, A79
- 980 Dobbie, P. D., Lodieu, N., & Sharp, R. G. 2010,
 981 *MNRAS*, 409, 1002
- 982 Douglas, S. T., Agüeros, M. A., Covey, K. R., & Kraus,
 983 A. 2017, *ApJ*, 842, 83
- 984 Douglas, S. T., Pérez Chávez, J., Cargile, P. A., et al.
 985 2021, [10.5281/zenodo.5131306](https://doi.org/10.5281/zenodo.5131306)
- 986 Eggen, O. J. 1968, *ApJ*, 152, 77
- 987 Ehrenreich, D., Bourrier, V., Wheatley, P. J., et al. 2015,
 988 *Nature*, 522, 459
- 989 Esplin, T. L., & Luhman, K. L. 2019, *AJ*, 158, 54
- 990 Feinstein, A. D., Montet, B. T., Johnson, M. C., et al.
 991 2021, arXiv:2107.01213 [astro-ph]
- 992 Foreman-Mackey, D. 2016, *Journal of Open Source
 993 Software*, 1, 24
- 994 Foreman-Mackey, D., Czekala, I., Luger, R., et al. 2020,
 995 exoplanet-dev/exoplanet v0.2.6
- 996 Fulton, B. J., Petigura, E. A., Howard, A. W., et al.
 997 2017, *AJ*, 154, 109
- 998 Fürnkranz, V., Meingast, S., & Alves, J. 2019, *A&A*,
 999 624, L11
- 1000 Gagné, J., David, T. J., Mamajek, E. E., et al. 2020,
 1001 *ApJ*, 903, 96

- 1002 Gagné, J., & Faherty, J. K. 2018, *ApJ*, 862, 138
- 1003 Gagné, J., Roy-Loubier, O., Faherty, J. K., Doyon, R.,
1004 & Malo, L. 2018a, *ApJ*, 860, 43
- 1005 Gagné, J., Mamajek, E. E., Malo, L., et al. 2018b, *ApJ*,
1006 856, 23
- 1007 Gagné, J., David, T. J., Mamajek, E. E., et al. 2020,
1008 *ApJ*, 903, 96
- 1009 Gaia Collaboration, Babusiaux, C., van Leeuwen, F.,
1010 et al. 2018a, *A&A*, 616, A10
- 1011 Gaia Collaboration, Brown, A. G. A., Vallenari, A.,
1012 et al. 2018b, *A&A*, 616, A1
- 1013 —. 2021a, *A&A*, 649, A1
- 1014 Gaia Collaboration, Smart, R. L., Sarro, L. M., et al.
1015 2021b, *A&A*, 649, A6
- 1016 Gelman, A., & Rubin, D. B. 1992, *Statistical Science*, 7,
1017 457, publisher: Institute of Mathematical Statistics
- 1018 Gibson, S. R., Howard, A. W., Marcy, G. W., et al. 2016,
1019 in SPIE Conference Series, Vol. 9908, *Ground-based*
1020 and *Airborne Instrumentation for Astronomy VI*, ed.
1021 C. J. Evans, L. Simard, & H. Takami, 990870
- 1022 Gillen, E., Briegal, J. T., Hodgkin, S. T., et al. 2020,
1023 *MNRAS*, 492, 1008
- 1024 Ginsburg, A., Sipocz, B., Madhura Parikh, et al. 2018,
1025 *Astropy/Astroquery: V0.3.7 Release*
- 1026 Ginzburg, S., Schlichting, H. E., & Sari, R. 2018,
1027 *MNRAS*, 476, 759
- 1028 Goldman, B., Röser, S., Schilbach, E., Moór, A. C., &
1029 Henning, T. 2018, *ApJ*, 868, 32
- 1030 Guerrero, N. M., Seager, S., Huang, C. X., et al. 2021,
1031 *ApJS*, 254, 39
- 1032 Günther, M. N., Zhan, Z., Seager, S., et al. 2020, *AJ*,
1033 159, 60
- 1034 Gupta, A., & Schlichting, H. E. 2020, *MNRAS*, 493,
1035 792
- 1036 Hattori, S., Foreman-Mackey, D., Hogg, D. W., et al.
1037 2021, arXiv e-prints, arXiv:2106.15063
- 1038 Hippke, M., David, T. J., Mulders, G. D., & Heller, R.
1039 2019, *AJ*, 158, 143
- 1040 Hirano, T., Suto, Y., Taruya, A., et al. 2010, *ApJ*, 709,
1041 458
- 1042 Hirano, T., Suto, Y., Winn, J. N., et al. 2011, *ApJ*, 742,
1043 69
- 1044 Hoffman, M. D., & Gelman, A. 2014, *Journal of
1045 Machine Learning Research*, 15, 1593
- 1046 Holczer, T., Shporer, A., Mazeh, T., et al. 2015, *ApJ*,
1047 807, 170
- 1048 Holczer, T., Mazeh, T., Nachmani, G., et al. 2016,
1049 *ApJS*, 225, 9
- 1050 Howard, A. W., Johnson, J. A., Marcy, G. W., et al.
1051 2010, *ApJ*, 721, 1467
- 1052 Howell, S. B., Everett, M. E., Sherry, W., Horch, E., &
1053 Ciardi, D. R. 2011, *AJ*, 142, 19
- 1054 Ikoma, M., & Hori, Y. 2012, *ApJ*, 753, 66
- 1055 Ilin, E., Schmidt, S. J., Poppenhöger, K., et al. 2021,
1056 *A&A*, 645, A42
- 1057 Jones, E., Oliphant, T., Peterson, P., et al. 2001, Open
1058 source scientific tools for Python
- 1059 Kass, R. E., & Raftery, A. E. 1995, *Journal of the
1060 American Statistical Association*, 90, 773
- 1061 Kerr, R. M. P., Rizzuto, A. C., Kraus, A. L., & Offner,
1062 S. S. R. 2021, *ApJ*, 917, 23
- 1063 Kharchenko, N. V., Piskunov, A. E., Schilbach, E.,
1064 Röser, S., & Scholz, R.-D. 2013, *A&A*, 558, A53
- 1065 King, G. W., & Wheatley, P. J. 2021, *MNRAS*, 501, L28
- 1066 Kipping, D. M. 2010, *MNRAS*, 408, 1758
- 1067 Kipping, D. M. 2013, *MNRAS*, 435, 2152
- 1068 Kite, E. S., Fegley, Jr., B., Schaefer, L., & Ford, E. B.
1069 2020, *ApJ*, 891, 111
- 1070 Klein, B., & Donati, J.-F. 2020, *MNRAS*, 493, L92
- 1071 Kounkel, M., & Covey, K. 2019, *AJ*, 158, 122
- 1072 Kounkel, M., Covey, K., & Stassun, K. G. 2020, *AJ*,
1073 160, 279
- 1074 Kounkel, M., Covey, K., Suárez, G., et al. 2018, *AJ*,
1075 156, 84
- 1076 Kounkel, M., Covey, K., Suárez, G., et al. 2018, *AJ*,
1077 156, 84
- 1078 Kraus, A. L., Ireland, M. J., Huber, D., Mann, A. W., &
1079 Dupuy, T. J. 2016, *AJ*, 152, 8
- 1080 Kraus, A. L., Shkolnik, E. L., Allers, K. N., & Liu,
1081 M. C. 2014, *AJ*, 147, 146
- 1082 Lallement, R., Capitanio, L., Ruiz-Dern, L., et al. 2018,
1083 *A&A*, 616, A132
- 1084 Lindegren, L., Bastian, U., Biermann, M., et al. 2021,
1085 *A&A*, 649, A4
- 1086 Lomb, N. R. 1976, *Astrophysics and Space Science*, 39,
1087 447
- 1088 Lopez, E. D., Fortney, J. J., & Miller, N. 2012, *ApJ*,
1089 761, 59
- 1090 Luger, R., Agol, E., Foreman-Mackey, D., et al. 2019,
1091 *AJ*, 157, 64
- 1092 Mann, A. W., Newton, E. R., Rizzuto, A. C., et al. 2016,
1093 *AJ*, 152, 61
- 1094 Mann, A. W., Johnson, M. C., Vanderburg, A., et al.
1095 2020, *AJ*, 160, 179
- 1096 Martioli, E., Hébrard, G., Correia, A. C. M., Laskar, J.,
1097 & Lecavelier des Etangs, A. 2021, *A&A*, 649, A177
- 1098 Masuda, K. 2015, *ApJ*, 805, 28
- 1099 Mazeh, T., Holczer, T., & Shporer, A. 2015, *ApJ*, 800,
1100 142
- 1101 McCann, J., Murray-Clay, R. A., Kratter, K., &
1102 Krumholz, M. R. 2019, *ApJ*, 873, 89

- 1103 McKinney, W. 2010, in Proceedings of the 9th Python
 1104 in Science Conference, ed. S. van der Walt &
 1105 J. Millman, 51
- 1106 McQuillan, A., Mazeh, T., & Aigrain, S. 2014, *ApJS*,
 1107 211, 24
- 1108 Meibom, S., Mathieu, R. D., & Stassun, K. G. 2007,
 1109 *ApJL*, 665, L155
- 1110 Meibom, S., Barnes, S. A., Latham, D. W., et al. 2011,
 1111 *ApJL*, 733, L9
- 1112 Meibom, S., Torres, G., Fressin, F., et al. 2013, *Nature*,
 1113 499, 55
- 1114 Meingast, S., & Alves, J. 2019, *A&A*, 621, L3
- 1115 Meingast, S., Alves, J., & Rottensteiner, A. 2021, *A&A*,
 1116 645, A84
- 1117 Montet, B. T., Tovar, G., & Foreman-Mackey, D. 2017,
 1118 *ApJ*, 851, 116
- 1119 Montet, B. T., Feinstein, A. D., Luger, R., et al. 2020,
 1120 *AJ*, 159, 112
- 1121 Morris, B. M. 2020, *ApJ*, 893, 67
- 1122 Morton, T. D., Bryson, S. T., Coughlin, J. L., et al.
 1123 2016, *ApJ*, 822, 86
- 1124 Narita, N., Fukui, A., Yamamuro, T., et al. 2020, in
 1125 *SPIE Conference Series*, 114475K
- 1126 Newton, E. R., Mann, A. W., Tofflemire, B. M., et al.
 1127 2019, *ApJ*, 880, L17
- 1128 Oh, S., Price-Whelan, A. M., Hogg, D. W., Morton,
 1129 T. D., & Spergel, D. N. 2017, *AJ*, 153, 257
- 1130 Owen, J. E. 2020, *MNRAS*, 498, 5030
- 1131 Owen, J. E., & Wu, Y. 2013, *ApJ*, 775, 105
 1132 —. 2016, *ApJ*, 817, 107
 1133 —. 2017, *ApJ*, 847, 29
- 1134 Palle, E., Oshagh, M., Casasayas-Barris, N., et al. 2020,
 1135 *A&A*, 643, 25
- 1136 Pavlidou, T., Scholz, A., & Teixeira, P. S. 2021,
 1137 *MNRAS*, 503, 3232
- 1138 Pecaut, M. J., & Mamajek, E. E. 2013, *ApJS*, 208, 9
- 1139 Pecaut, M. J., & Mamajek, E. E. 2016, *MNRAS*, 461,
 1140 794
- 1141 Plavchan, P., Barclay, T., Gagné, J., et al. 2020, *Nature*,
 1142 582, 497
- 1143 Poppenhaeger, K., Ketzer, L., & Mallonn, M. 2021,
 1144 *MNRAS*, 500, 4560
- 1145 Randich, S., Tognelli, E., Jackson, R., et al. 2018, *A&A*,
 1146 612, A99
- 1147 Ratzenböck, S., Meingast, S., Alves, J., Möller, T., &
 1148 Bomze, I. 2020, *A&A*, 639, A64
- 1149 Rebull, L. M., Stauffer, J. R., Bouvier, J., et al. 2016,
 1150 *AJ*, 152, 113
- 1151 Reinhold, T., & Hekker, S. 2020, *A&A*, 635, A43
- 1152 Ricker, G. R., Winn, J. N., Vanderspek, R., et al. 2015,
 1153 *JATIS*, 1, 014003
- 1154 Rizzuto, A. C., Mann, A. W., Vanderburg, A., Kraus,
 1155 A. L., & Covey, K. R. 2017, *AJ*, 154, 224
- 1156 Rizzuto, A. C., Newton, E. R., Mann, A. W., et al. 2020,
 1157 *AJ*, 160, 33
- 1158 Roccatagliata, V., Franciosini, E., Sacco, G. G.,
 1159 Randich, S., & Sicilia-Aguilar, A. 2020, *A&A*, 638,
 1160 A85
- 1161 Roettenbacher, R. M., Monnier, J. D., Korhonen, H.,
 1162 et al. 2017, *ApJ*, 849, 120
- 1163 Rogers, J. G., & Owen, J. E. 2021, *Monthly Notices of
 1164 the Royal Astronomical Society*, 503, 1526, aDS
 1165 Bibcode: 2021MNRAS.503.1526R
- 1166 Röser, S., & Schilbach, E. 2020, *A&A*, 638, A9
- 1167 Salvatier, J., Wieckiâ, T. V., & Fonnesbeck, C. 2016,
 1168 PyMC3: Python probabilistic programming
 1169 framework
- 1170 Scargle, J. D. 1982, *ApJ*, 263, 835
- 1171 Scott, N. J., Howell, S. B., Horch, E. P., & Everett,
 1172 M. E. 2018, *PASP*, 130, 054502
- 1173 Scott, N. J., Howell, S. B., Gnilka, C. L., et al. 2021,
 1174 *Frontiers in Astronomy and Space Sciences*, 8, 138
- 1175 Seifahrt, A., Stürmer, J., Bean, J. L., & Schwab, C.
 1176 2018, in *SPIE Conference Series*, Vol. 10702,
 1177 *Ground-based and Airborne Instrumentation for
 1178 Astronomy VII*, ed. C. J. Evans, L. Simard, &
 1179 H. Takami, 107026D
- 1180 Shapiro, A. I., Solanki, S. K., Krivova, N. A., Yeo,
 1181 K. L., & Schmutz, W. K. 2016, *A&A*, 589, A46
- 1182 Shporer, A., Zhou, G., Vanderburg, A., et al. 2017,
 1183 *ApJL*, 847, L18
- 1184 Skrutskie, M. F., Cutri, R. M., Stiening, R., et al. 2006,
 1185 *AJ*, 131, 1163
- 1186 Smith, J. C., Morris, R. L., Jenkins, J. M., et al. 2016,
 1187 *PASP*, 128, 124501
- 1188 Smith, J. C., Stumpe, M. C., Jenkins, J. M., et al. 2017,
 1189 *Kepler Science Document*, 8
- 1190 Soderblom, D. R., Hillenbrand, L. A., Jeffries, R. D.,
 1191 Mamajek, E. E., & Naylor, T. 2014, *Protostars and
 1192 Planets VI*, 219
- 1193 Spake, J. J., Sing, D. K., Evans, T. M., et al. 2018,
 1194 *Nature*, 557, 68
- 1195 Stassun, K. G., Oelkers, R. J., Paegert, M., et al. 2019,
 1196 *AJ*, 158, 138
- 1197 Stauffer, J., Rebull, L., Bouvier, J., et al. 2016, *AJ*, 152,
 1198 115
- 1199 Stauffer, J. R., Hartmann, L. W., Prosser, C. F., et al.
 1200 1997, *ApJ*, 479, 776
- 1201 Stefansson, G., Mahadevan, S., Maney, M., et al. 2020,
 1202 *AJ*, 160, 192
- 1203 Stephenson, C. B. 1959, *PASP*, 71, 145

- 1204 Strassmeier, K. G. 2009, *Astronomy and Astrophysics Review*, 17, 251
- 1205 Tenenbaum, P., Christiansen, J. L., Jenkins, J. M., et al. 2012, *ApJS*, 199, 24
- 1206 Theano Development Team. 2016, arXiv e-prints, [abs/1605.02688](https://arxiv.org/abs/1605.02688)
- 1207 Thompson, S. E., Coughlin, J. L., Hoffman, K., et al. 2018, *ApJS*, 235, 38
- 1208 Tian, H.-J. 2020, *ApJ*, 904, 196
- 1209 Tofflemire, B. M., Rizzuto, A. C., Newton, E. R., et al. 2021, *AJ*, 161, 171
- 1210 Ujjwal, K., Kartha, S. S., Mathew, B., Manoj, P., & Narang, M. 2020, *AJ*, 159, 166
- 1211 Van Eylen, V., Agentoft, C., Lundkvist, M. S., et al. 2018, *MNRAS*, 479, 4786
- 1212 Van Eylen, V., Albrecht, S., Huang, X., et al. 2019, *AJ*, 157, 61
- 1213 Villa Vélez, J. A., Brown, A. G. A., & Kenworthy, M. A. 2018, *RNAAS*, 2, 58
- 1223 Vissapragada, S., Knutson, H. A., Jovanovic, N., et al. 2020, *AJ*, 159, 278
- 1224 Vogt, S. S., Allen, S. L., Bigelow, B. C., et al. 1994, SPIE Conference Series, ed. D. L. Crawford & E. R. Craine, Vol. 2198
- 1225 Walkowicz, L. M., & Basri, G. S. 2013, *MNRAS*, 436, 1883, arXiv: 1309.2159
- 1226 Wang, L., & Dai, F. 2019, *ApJL*, 873, L1
- 1227 Wenger, M., Ochsenbein, F., Egret, D., et al. 2000, *A&AS*, 143, 9
- 1228 Wirth, C. P., Zhou, G., Quinn, S. N., et al. 2021, *ApJL*, 917, L34
- 1229 Wu, Y. 2019, *ApJ*, 874, 91
- 1230 Yee, S. W., Petigura, E. A., & von Braun, K. 2017, *ApJ*, 836, 77
- 1231 Yelda, S., Lu, J. R., Ghez, A. M., et al. 2010, *ApJ*, 725, 331
- 1232 Zari, E., Hashemi, H., Brown, A. G. A., Jardine, K., & de Zeeuw, P. T. 2018, *A&A*, 620, A172
- 1233 Zhou, G., Winn, J. N., Newton, E. R., et al. 2020, *ApJ*, 892, L21
- 1234 Zhou, G., Quinn, S. N., Irwin, J., et al. 2021, *AJ*, 161, 2

1245

APPENDIX

1246

A. YOUNG, AGE-DATED, AND AGE-DATEABLE STAR COMPILED

1247 The v0.6 CDIPS target catalog (Table 3) includes stars that are young, age-dated, and age-dateable. By
 1248 “age-dateable”, we mean that the stellar age should be measurable at greater precision than that of a typical
 1249 FGK field star, through either isochronal, gyrochronal, or spectroscopic techniques. As in Bouma et al.
 1250 (2019), we collected stars that met these criteria from across the literature. Table 4 gives a list of the studies
 1251 included, and brief summary statistics. The age measurement methodologies adopted by each study differ: in
 1252 many, spatial and kinematic clustering has been performed on the Gaia data, and ensemble isochrone fitting
 1253 of the resulting clusters has been performed (typically focusing on the turn-off). In other studies however,
 1254 the claim of youth is based on the location of a single star in the color-absolute magnitude diagram, or on
 1255 spectroscopic information.

1256 One major change in Table 3 relative to the earlier iteration from Bouma et al. (2019) is that the extent
 1257 of Gaia-based analyses has now matured to the point that we can neglect pre-Gaia cluster memberships,
 1258 except for a few cases with spectroscopically confirmed samples of age-dated stars. The membership lists for
 1259 instance of Kharchenko et al. (2013) and Dias et al. (2014) (MWSC and DAML) are no longer required. This
 1260 is helpful for various post-processing projects, since the field star contamination rates were typically much
 1261 higher in these catalogs than in the newer Gaia-based catalogs.

1262 The most crucial parameters of a given star for our purposes are the Gaia DR2 `source_id`, the cluster or
 1263 group name (`cluster`), and the age. Given the hierarchical nature of many stellar associations, we do not
 1264 attempt to resolve the cluster names to a single unique string. The Orion complex for instance can be divided
 1265 into almost one hundred kinematic subgroups (Kounkel et al. 2018). Based on Figure 1, the δ Lyr cluster may
 1266 also be part of a similar hierarchical association. Similar complexity applies to the problem of determining
 1267 homogeneous ages, which we do not attempt to resolve. Instead, we simply merged the cluster names and
 1268 ages reported by various authors into a comma-separated string.

1269 This means that the `age` column can be null, for cases in which the original authors did not report an age,
 1270 or for which a reference literature age was not readily available. Nonetheless, since we do prefer stars with
 1271 known ages, we made a few additional efforts to populate this column. When available, the age provenance
 1272 is from the original analysis of the cluster. In a few cases however we adopted other ages when string-
 1273 based cross-matching on the cluster name was straightforward. In particular, we used the ages determined
 1274 by Cantat-Gaudin et al. (2020) to assign ages to the clusters from Gaia Collaboration et al. (2018a), Cantat-
 1275 Gaudin et al. (2018), Castro-Ginard et al. (2020), and Cantat-Gaudin & Anders (2020).

1276 The catalogs we included for which ages were not immediately available were those of Cotten & Song
 1277 (2016), Oh et al. (2017), Zari et al. (2018), Gagné et al. (2018a), Gagné et al. (2018b), Gagné & Faherty
 1278 (2018), and Ujjwal et al. (2020). While in principle the moving group members discussed by Gagné et al.
 1279 (2018a,b); Gagné & Faherty (2018) and Ujjwal et al. (2020) have easily associated ages, our SIMBAD cross-
 1280 match did not retain the moving group identifiers given by those studies, which should therefore be recovered
 1281 using tools such as BANYAN Σ (Gagné et al. 2018b). We also included the SIMBAD object identifiers `TT*`,
 1282 `Y*O,Y*?`, `TT?`, and `pMS*`. Finally, we included every star in the NASA Exoplanet Archive planetary system
 1283 (`ps`) table that had a Gaia identifier available (Akeson et al. 2013). If the age had finite uncertainties, we also
 1284 included it, since stellar ages determined through the combination of isochrone-fitting and transit-derived
 1285 stellar densities typically have higher precision than from isochrones alone.

1286 For any of the catalogs for which Gaia DR2 identifiers were not available, we either followed the spa-
 1287 tial (plus proper-motion) cross-matching procedures described in Bouma et al. (2019), or else we pulled the
 1288 Gaia DR2 source identifiers associated with the catalog from SIMBAD. We consequently opted to drop the
 1289 `ext_catalog_name` and `dist` columns maintained in Bouma et al. (2019), as these were only popu-
 1290 lated for a small number of stars. The technical manipulations for the merging, cleaning, and joining were
 1291 performed using pandas (McKinney 2010). The eventual cross-match (using the Gaia DR2 `source_id`)
 1292 against the Gaia DR2 archive was performed asynchronously on the Gaia archive website.

1293

B. THE TRANSIT ASYMMETRY

1294

B.1. How Robust is the Asymmetric Transit?

1295 As a means of exploring the robustness of the transit asymmetry, Figures 9, 10, and 11 show the Kepler data
 1296 binned in three ways: over Kepler quarters, Julian years, and quartiles of local slope. Over Kepler quarters
 1297 (Figure 9), Quarter 6 shows the strongest asymmetry: a deviation of about 3 ppt from expectation. Quarter

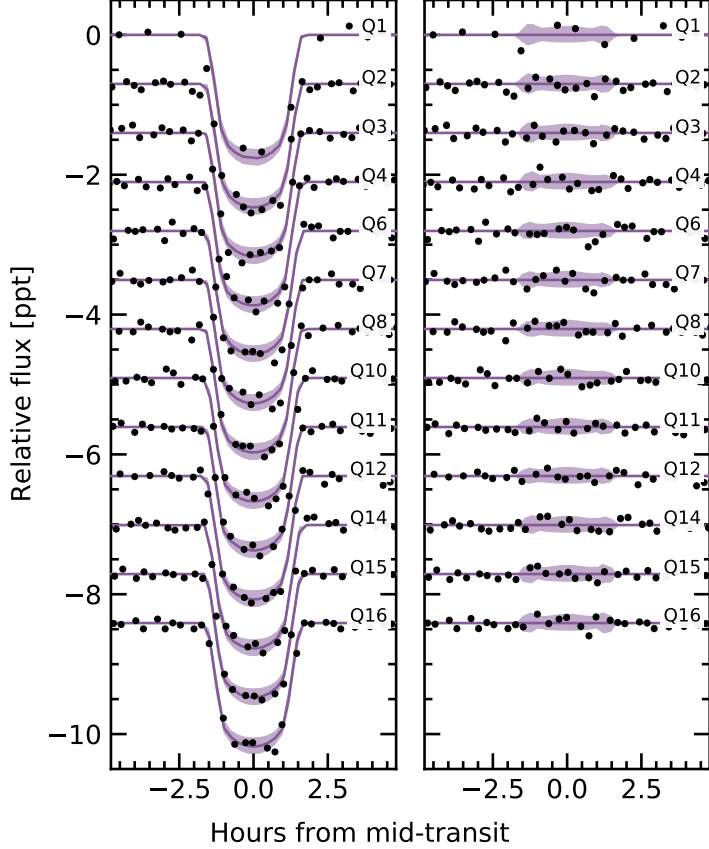


Figure 9. Transit model residuals through time (binned by Kepler quarter). *Left:* Phase-folded transit of Kepler 1627b, with stellar variability removed. Black points are binned to 20 minute intervals. The 2σ model uncertainties and the maximum *a posteriori* model are shown as the faint purple band, and the dark purple line. *Right:* As on the left, with the transit removed.

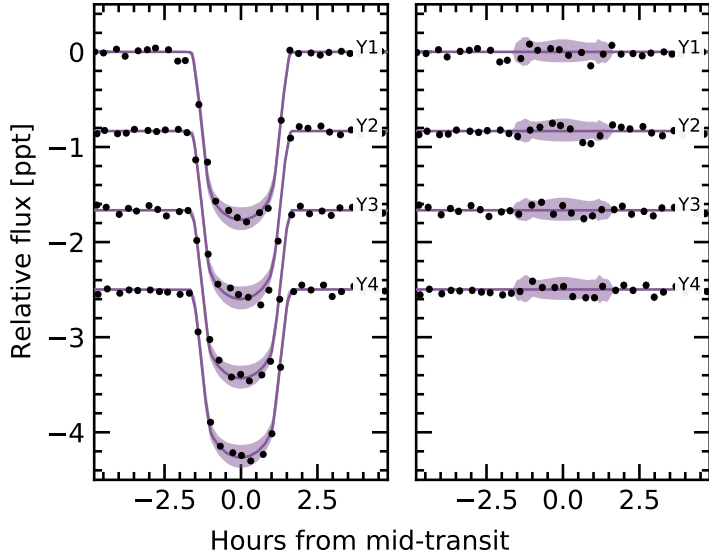


Figure 10. Transit model residuals through time (binned by year of observation). *Left:* Phase-folded transit of Kepler 1627b, with stellar variability removed. Points and models are as in Figure 9. *Right:* As on the left, with the transit removed.

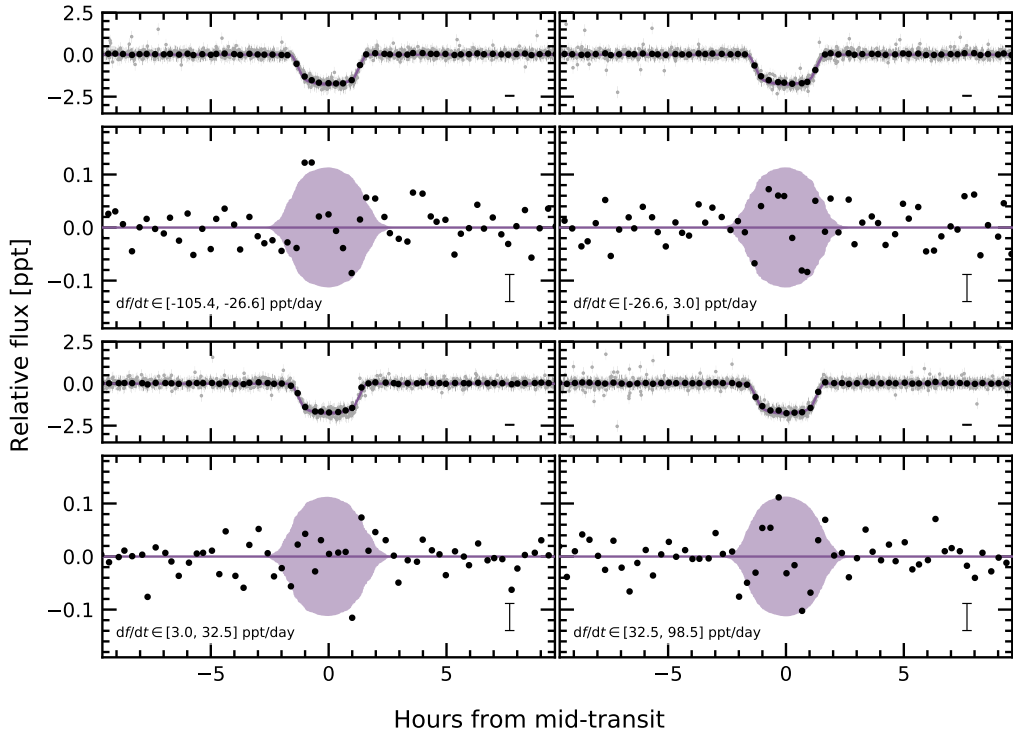


Figure 11. Transit models and residuals, binned by quartiles in the local slope of the light curve. Representative uncertainties for the black points (binned at 20 minute intervals) are shown in the lower right of each panel. A similar transit asymmetry to that shown in Figure 5 seems to be present in three of the four bins.

1298 7 shows an anomaly at roughly the same transit phase. Year 2 correspondingly shows the strongest anomaly
 1299 out of any year in Figure 10; the asymmetry is visually apparent however in each of the four years.

1300 To bin by quartiles in local slope, we used our measurements of the local linear slopes in each of the
 1301 observed transit windows (144 transits total). Four outlier transits were removed, leaving 140 transits. These
 1302 were then divided into quartiles, so that each panel shows 35 transits binned together. The exact light curve
 1303 slope intervals are listed in the lower left panels of Figure 11. Binned by local slope quartiles (Figure 11),
 1304 the asymmetry is visually present in three of the four quartiles: the only bin in which it does not appear is
 1305 $df/dt \in [3.0, 32.5] \text{ ppt day}^{-1}$.

1306 Within the theory presented by Mazeh et al. (2015), unresolved starspot crossings cause the weak correlation
 1307 between TTVs and the local light curve slope (Figure 6). In this model, we would expect the light curves
 1308 with the most negative local slopes to have the largest positive TTVs, due to spot crossing events during the
 1309 latter half of transit. The upper-left panel of Figure 11 agrees with this expectation. However, we would also
 1310 expect the sign of the effect to reverse when considering the most positive local slopes (most negative TTVs).
 1311 The lower-right panel of Figure 11 contradicts this expectation: the residual in both cases maintains the same
 1312 parity! On the one hand, this shows that the residual is not dependent on the local light curve slope, which
 1313 lowers the likelihood that it might be an artifact of our detrending methods. On the other, it raises the question
 1314 of whether unresolved starspot crossings are indeed the root cause of the correlation shown in Figure 6. While
 1315 we do not have a solution to this contradiction, the injection-recovery tests discussed in Section 4.1.3 provide
 1316 some assurance that the TTV-slope correlation is not simply a systematic artifact.

B.2. Interpretation

1318 The transit asymmetry seems robust against most methods of binning the data, though with some caveats
 1319 (e.g., the “middle quartile” in local flux, $df/dt \in [3.0, 32.5] \text{ ppt day}^{-1}$, where the asymmetry does not appear).
 1320 Nonetheless, if the asymmetric were systematic we might expect its parity to reverse as a function of the sign
 1321 of the local slope, and it does not. We therefore entertained four possible astrophysical explanations: gravity
 1322 darkening, transit timing variations, spot-crossing events, and a persistent asymmetric dusty outflow.

1323 Gravity darkening is based on the premise that the rapidly rotating star is oblate, and brighter near the
 1324 poles than the equator (e.g., Masuda 2015). The fractional transit shape change due to gravity darkening
 1325 is on the order of $(P_{\text{break}}/P_{\text{rot}})^2$, for P_{break} the break-up rotation period, and P_{rot} the rotation period. Using

1326 the parameters from Table 2, this yields an expected 0.14% distortion of the ≈ 1.8 ppt transit depth: *i.e.*, an
 1327 absolute deviation of ≈ 2.5 ppm. The observed residual has a semi-amplitude of ≈ 50 ppm. Since the expected
 1328 signal is smaller than the observed anomaly by over an order of magnitude, gravity darkening seems to be an
 1329 unlikely explanation.

1330 The scenario of transit timing variations (TTVs) producing the asymmetry seems unlikely because the transit
 1331 timing variations we do observe are correlated with the local light curve slope, which increases roughly as
 1332 much as it decreases. From our analysis, the mean TTV and its standard deviation are 0.66 ± 5.53 min;
 1333 similarly the mean local slope and its standard deviation are 0.59 ± 45.50 ppt day $^{-1}$. There is therefore little
 1334 expectation for TTVs to produce the asymmetry. A separate line of argument comes from Figure 11. If the
 1335 local slope were essential to producing the transit asymmetry, we would expect that in the largest df/dt bin,
 1336 $df/dt \in [3.0, 32.5]$ ppt day $^{-1}$, the sign of the asymmetry would reverse. We do not see evidence for this being
 1337 the case.

1338 The third and related possibility is that of starspot crossings. Young stars have higher spot-covering fractions
 1339 than old stars (*e.g.*, Morris 2020). Young solar-type stars may also host dark starspots at high stellar
 1340 latitudes (*e.g.*, EK Dra; Strassmeier 2009), though interferometric imaging of spotted giant stars has shown
 1341 different starspot latitude distributions than those inferred from Doppler imaging (Roettenbacher et al. 2017).
 1342 Regardless, for any spot-crossing anomalies to add coherently over the 140 Kepler transits, it seems likely
 1343 that we would need either for spots to be persistent at a particular latitude (and for the planetary orbit to be
 1344 somewhat misaligned), or for a “stroboscopic” longitudinal phasing (*e.g.*, Dai et al. 2018). For our system,
 1345 $P_{\text{orb}}/P_{\text{rot}} \approx 2.76$, which means that every 4 transits and 11 stellar rotations, the planet crosses over roughly the
 1346 same stellar longitude, which might enable the necessary phasing if the spot-groups are large and long-lived.
 1347 Unfortunately, the S/N per Kepler transit is ≈ 8 , which renders individual spot-crossing events unresolved.
 1348 This explanation seems marginally plausible, mainly because the expected spot-crossing anomaly amplitudes
 1349 (≈ 100 ppm) resemble the observed amplitude of the asymmetry (≈ 50 ppm). One issue with this explanation
 1350 however is that there is no reason to expect starspot crossing events to last exactly half the transit duration.

1351 A persistent feature of the planet itself might therefore be needed to explain the transit asymmetry. An
 1352 asymmetric outflow from the planet’s atmosphere could at least geometrically meet the requirements (*e.g.*,
 1353 McCann et al. 2019). To explain the asymmetric transit, a small, dense component would lead the planet,
 1354 and a long, more rarefied (and variable) component would trail it. This might also explain the slight flux
 1355 decrement visible for ~ 1 hour pre-ingress (Figure 5). The amplitude of the asymmetry is roughly in line
 1356 with theoretical expectations for dusty outflows (Wang & Dai 2019), and based on the planet’s size, its mass
 1357 is likely in a regime where such outflows are possible. Out of the four explanations discussed, this one at
 1358 least theoretically seems the most plausible. By composition, the expectation would be that the envelope
 1359 is mostly hydrogen and helium gas, with a dust or haze component providing the broadband opacity in the
 1360 Kepler bandpass. A natural path for testing this idea would be to observe additional transits of the planet in
 1361 hydrogen absorption, metastable helium absorption, or across a broad wavelength range in the near-infrared.

1362 C. SPECTROSCOPY AND PHOTOMETRY DURING THE TRANSIT OF 2021 AUG 7

1363 We used the ephemeris of Holczer et al. (2016) to observe a transit of Kepler 1627Ab on the night of
 1364 2021 Aug 7 both spectroscopically and photometrically. We used the HIRES echelle spectrograph at the
 1365 Keck-I telescope and the MuSCAT3 photometer at Haleakalā Observatory on Maui, HI (Narita et al. 2020).
 1366 For the HIRES wavelength calibration, we used the iodine cell, and extracted the 1-D spectra using the
 1367 standard California Planet Survey pipeline (Howard et al. 2010). Given the faintness of the target ($V =$
 1368 13.1), we observed using the C2 decker, which yielded an instrument resolution of $\approx 50,000$. The airmass
 1369 ranged between 1.1 and 2.2 from the start through the end of observations; the seeing ranged from $1.^{\prime\prime}1$ at
 1370 the beginning to $1.^{\prime\prime}5$ at the end. The HIRES exposure time was set at ≈ 15 minutes in order to resolve the
 1371 2.8 hour transit event, which yielded a S/N per resolution element of ≈ 75 (low for precision radial velocity
 1372 standards). For the MuSCAT3 observations, we observed simultaneously across the *griz* bands. The exposure
 1373 times in each bandpass ranged between 23 and 46 seconds, and were chosen in order to yield a S/N in the
 1374 peak pixel that exceeded 130 while also preventing saturation. Performing aperture photometry on the latter
 1375 image stack yielded the data given in Table 5.

1376 We considered two approaches to measuring the velocities: in the first, hereafter “Method 1”, we cross-
 1377 correlated against a template found via spectral classification with SpecMatch-Emp (Yee et al. 2017). In
 1378 “Method 2”, we used a high S/N template of V1298 Tau. Although V1298 Tau is cooler than Kepler 1627A
 1379 by ≈ 500 K, it has a comparable amount of line-broadening ($v \sin i = 23$ km s $^{-1}$), and a comparable level of
 1380 stellar activity. The mean and standard deviation of the internal RV uncertainties averaged over all epochs
 1381 were 16.2 ± 1.1 m s $^{-1}$ from Method 1, and 12.6 ± 0.6 m s $^{-1}$ from Method 2. The corresponding time-averaged

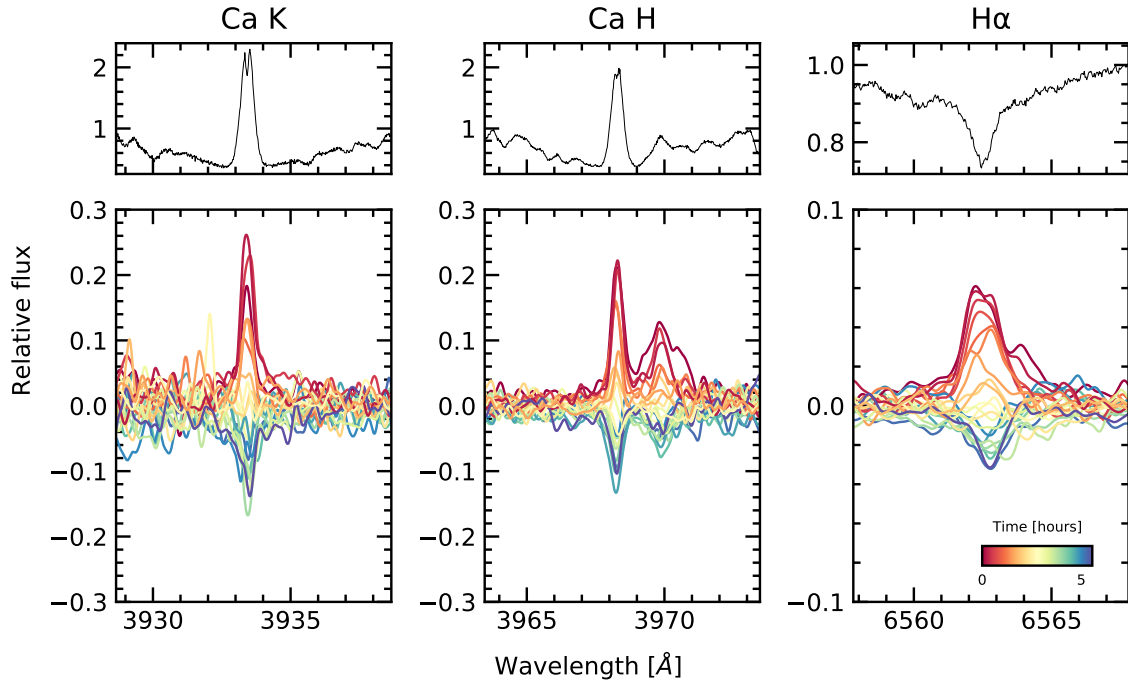


Figure 12. Spectroscopic activity indicators during the transit of 2021 Aug 7. The *top panels* show the median line profiles Ca K, Ca H, and H α line profiles from the HIRES spectra. The *lower panels* show the differences of each individual spectrum relative to the median spectrum. The bump in the red wing of Ca H is He ϵ . The spectra in the lower panels are smoothed for visualization purposes.

reduced χ^2 from the template match was 1.57 ± 0.04 (Method 1) and 1.30 ± 0.02 (Method 2). Given these diagnostics, we adopted the velocities from the second approach, which are reported in Table 6.

Figure 7 shows the results. The MuSCAT3 photometry shows the expected starspot trend, along with the transit and what is likely a chromatic starspot crossing event at JD – 2459433 = 0.955. The radial velocities decrease by $\approx 250 \text{ m s}^{-1}$ over the six hour window. This decrease in RV is correlated with a decrease in the S-indices derived from the Ca HK lines. One outlying RV point is apparent shortly before egress; it is temporally coincident with an outlying value in the S-index time series.

Overall, we expect the dominant trends in both the photometry and radial velocities to be caused by starspots on the stellar photosphere rotating into and out of view. The plasma in the leading and receding limbs of the stellar disk has an apparent line-of-sight velocity of $\pm 20 \text{ km s}^{-1}$. Over 10% of a rotation cycle ($P_{\text{rot}} = 2.6 \text{ days}$), spots near these limbs come into and out of view, modulate the stellar velocity profile, and can thereby produce the overall $\approx 250 \text{ m s}^{-1}$ trend. The Ca HK and H α emission profiles support this interpretation; Figure 12 shows that each line gradually decreases in intensity over the course of the six hour sequence.

The expectation however is for the starspot-induced signals to be smooth, at worst with contributions at $0.5 P_{\text{rot}}$ or $0.25 P_{\text{rot}}$ (Klein & Donati 2020). We therefore fitted the RVs using the Hirano et al. (2010, 2011) models for the Rossiter-McLaughlin (RM) effect, and allowed for an optional linear and quadratic trend in time to fit the $\approx 250 \text{ m s}^{-1}$ spot-induced trend. We followed the methodology developed by Stefansson et al. (2020). We allowed the sky-projected obliquity, the projected stellar equatorial velocity, and the Gaussian dispersion of the spectral lines to vary, and fixed the limb-darkening using the V-band tabulation from Claret & Bloemen (2011). We assumed a Gaussian prior on $v \sin i$ and a/R_* from Table 1, and also allowed for a white-noise jitter term to be added in quadrature to the measurement uncertainties. We used a 15 minute exposure time to numerically evaluate the model.

The quadratic model with the RM effect is shown in Figure 7; the jitter term is incorporated in the model uncertainties, but not the plotted measurement uncertainties. The plotted measurement uncertainties are the internal uncertainties on the RVs ($\approx 13 \text{ m s}^{-1}$), and are dominated by the $v \sin i$ broadening. However, between exposures, the RVs show significant additional scatter that is not captured by the slow quadratic trend. The

¹⁴⁰⁸ white-noise jitter for this particular model is $\sigma_{\text{RV}} = 27^{+6}_{-5} \text{ m s}^{-1}$, which is comparable to the expected RM
¹⁴⁰⁹ anomaly of $\Delta v_{\text{RM}} \approx f_{\text{LD}} \cdot \delta \cdot v \sin i \cdot \sqrt{1 - b^2} \approx 20 \text{ m s}^{-1}$, assuming a perfectly aligned orbit.

The presence of this additional scatter prevents a convincing detection of the RM effect. The reason can be understood via model comparison. If we compare the model with a quadratic trend and the RM effect against a model with a linear trend and the RM effect, or even a model with no RM effect at all, then the respective Bayesian Information Criterion (BIC) values are as follows.

$$\begin{aligned} \text{BIC} &= 227.1 \quad (\text{Quadratic + RM}) \\ \text{BIC} &= 231.1 \quad (\text{Linear + RM}) \\ \text{BIC} &= 221.4 \quad (\text{Only Quadratic}). \end{aligned} \quad (\text{C1})$$

¹⁴¹⁰ There is therefore no evidence to prefer the model with the RM effect against a model that only accounts
¹⁴¹¹ for the stellar variability. The “only quadratic” model does particularly well because it can inflate the jitter
¹⁴¹² term to account for scatter during the transit (even if the scatter contains astrophysics!), and it has fewer free
¹⁴¹³ parameters. However, we cannot justify a physical prior on the jitter term, because we do not understand
¹⁴¹⁴ the origin of the exposure-to-exposure scatter. As noted above, the velocity deviations from starspots are
¹⁴¹⁵ expected to have contributions at the stellar rotation frequency, or harmonics thereof. This jitter is present on
¹⁴¹⁶ the exposure timescale (15 minutes), which is only 0.4% of the stellar rotation period; it is not obvious that
¹⁴¹⁷ starspots would be the culprit.

¹⁴¹⁸ The amplitude of both the spot-induced trend and the jitter are somewhat larger than recent comparable
¹⁴¹⁹ measurements in systems such as AU Mic (Palle et al. 2020), DS Tuc (Montet et al. 2020; Zhou et al. 2020)
¹⁴²⁰ and TOI 942 (Wirth et al. 2021). One possible explanation for the jitter is that it is astrophysical in origin,
¹⁴²¹ and that it is caused by some novel process operating on the surface of Kepler 1627A. Another possibility
¹⁴²² is that our RV analysis underestimates our measurement uncertainties; in order to achieve the requisite time-
¹⁴²³ sampling the S/N per resolution element in our spectra was 70 to 80, which is lower than desired for deriving
¹⁴²⁴ high-precision velocities. In addition, the rapid rotation of the star could affect accuracy of the uncertainties
¹⁴²⁵ from the velocity extraction. Observations at higher S/N are necessary to distinguish these two possibilities,
¹⁴²⁶ and remain worthwhile in order to clarify the orbital geometry of Kepler 1627Ab. Useful next steps would
¹⁴²⁷ include transit observations with a stabilized spectrograph in the optical (e.g., Gibson et al. 2016; Seifahrt
¹⁴²⁸ et al. 2018), or in the near-infrared (e.g., Feinstein et al. 2021).

Table 5. MuSCAT3 photometry of Kepler 1627.

Time [BJD _{TDB}]	Rel. Flux	Rel. Flux Err.	Bandpass
2459433.829202	0.99719	0.00091	g
2459433.829324	0.99849	0.00112	r
2459433.829117	0.99611	0.00116	i
2459433.829406	0.99941	0.00136	z

NOTE— Table 5 is published in its entirety in a machine-readable format. Example entries are shown for guidance regarding form and content.

Table 6. Kepler 1627 radial velocities.

Time [BJD _{TDB}]	RV [m s^{-1}]	σ_{RV} [m s^{-1}]	S-value
2459433.801306	152.97	12.29	0.7355
2459433.812255	100.5	13.23	0.7434

NOTE— Table 6 is published in its entirety in a machine-readable format. Example entries are shown for guidance regarding form and content.

D. FLARE ANALYSIS

¹⁴³⁰ In addition to the 3.9 years of long cadence data,
¹⁴³¹ short cadence (1-minute) Kepler observations were
¹⁴³² acquired over 97.7 days during Quarter 15. The

¹⁴³³ short cadence light curve shows a higher rate of
¹⁴³⁴ flaring than visible in the long cadence data (Figure 13). We analyzed the short cadence light curve
¹⁴³⁵ and its flares according to the following procedure.
¹⁴³⁶

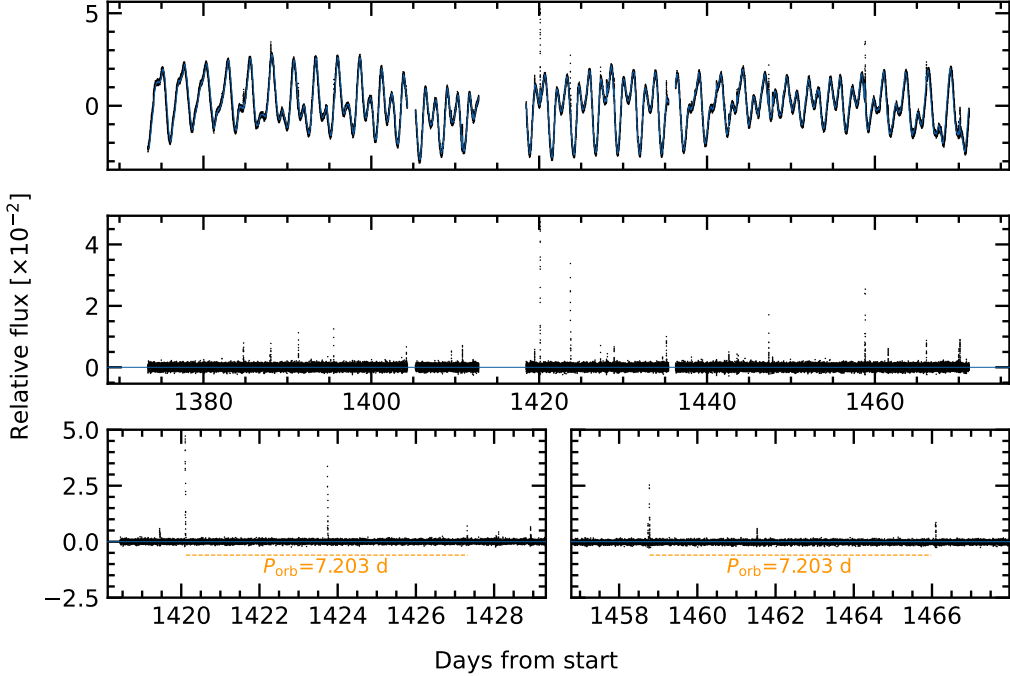


Figure 13. Flares in Kepler 1627. *Top:* The 1-minute cadence Kepler data (black points) is shown with a stellar variability model superposed (blue line). *Middle:* Residual after subtracting the stellar variability model. Flares appear as spikes. *Bottom:* Zooms of the brightest, and third-brightest flares. A timing coincidence – that both flares have “successors” approximately one planetary orbital period after the initial event – is emphasized.

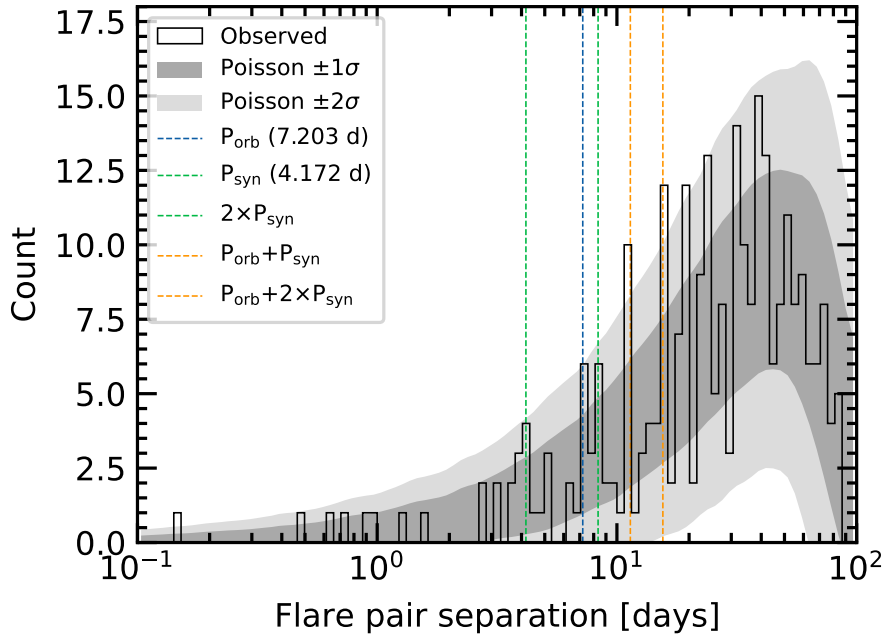


Figure 14. Statistics of inter-flare arrival times. 24 flares were recorded with amplitudes exceeding 0.5% over the 97.7 days of short cadence observations. The histogram of the time intervals between every possible pair of flares is shown in black. Some plausibly important timescales for star-planet interactions, namely the planetary orbital period and synodic period (the orbital period as seen from the rotating stellar frame) are shown along with their linear combinations. Monte Carlo draws from a Poisson distribution are shown with the gray bands. While peaks in the observed distribution do coincide with some of the “special periods”, the statistical evidence for a non-Poissonian process driving the flares does not clear the 5σ threshold.

- 1437 1. Fit the starspot-induced variability using a
 1438 Gaussian Process with a SHOTerm kernel,
 1439 a white-noise jitter term, and the mean flux.
- 1440 2. Select points more than twice the median ab-
 1441 solute deviation from the residual, and ex-
 1442 clude them from the light curve (these points
 1443 include the flares). Repeat Step 1.
- 1444 3. Using the residual from Step 2, identify all
 1445 flares, requiring them to be at least 20 ca-
 1446 dences apart, at least 7 median absolute de-
 1447 viations above the median baseline, and last-
 1448 ing at least 2 cadences in duration. Build the
 1449 mask spanning these times, from 5 minutes
 1450 before each flare begins to 2.5 minutes after
 1451 the final flare cadence. Repeat Step 1 a final
 1452 time.

1453 The final step of flare identification and fitting was
 1454 performed using `altaipony` (Davenport 2016;
 1455 Ilin et al. 2021). The analytic flare model is from
 1456 Davenport et al. (2014) and it parametrizes the flare
 1457 with a start time, an exponential lag time, and an
 1458 amplitude.

1459 There were $N_f = 24$ flares that exceeded 0.5% in
 1460 relative flux during the short cadence observations.
 1461 These 24 flares spanned a total of 6.5 hours (~ 15
 1462 minutes per flare). Inspecting the data, we noticed
 1463 a coincidence in the flare arrival times. The co-
 1464 incidence is that despite the low flare duty cycle,
 1465 one orbital period after the brightest flare, a second
 1466 flare followed. This and a similar event are shown
 1467 in Figure 13. The timing error is good to a $\approx 0.2\%$
 1468 difference from the orbital period, which given the
 1469 duty cycle seems *a priori* unlikely. If we consider
 1470 flares falling within 2% of the planet’s orbital pe-
 1471 riod after a previous flare, then 4 of the 24 flare
 1472 events have candidate “successors”.

1473 As with any coincidence, if one does not have a
 1474 firm prediction, it is difficult to assess whether a
 1475 surprise is statistically significant. Since our sur-
 1476prise was specifically at the inter-arrival time of
 1477 certain flares coinciding with special time inter-
 1478 vals, we performed the following analysis. First,
 1479 we considered all unordered pairs of flares. For
 1480 N flares there are $\binom{n}{2}$ such pairs (for our case,
 1481 276 pairs). We then compared the distribution of
 1482 the pair separations against that of a Poisson dis-
 1483 tribution. Specifically, we drew $N_f = 24$ samples
 1484 from a Poisson distribution with $\lambda = \Delta t / N_f$, for
 1485 $\Delta t = 97.7$ days the total duration of the observa-
 1486 tions, and repeated the draw 10^3 times with unique
 1487 random seeds.

1488 Figure 14 shows the results. The vertical lines
 1489 in the figure show the planetary orbital period,
 1490 the synodic period $P_{\text{syn}} = (P_{\text{rot}}^{-1} - P_{\text{orb}}^{-1})^{-1}$, and lin-
 1491 ear combinations thereof. The tidal period (half
 1492 the synodic period) is not shown. The bins are

1493 logarithmically spaced to give 100 bins between
 1494 the minimum and maximum ordinate values. The
 1495 gray bands express the range of values observed
 1496 from the Poissonian draws. While it does seem
 1497 like an odd coincidence for peaks in the observed
 1498 flare arrival time distribution to coincide with the
 1499 locations of these “special intervals”, the statisti-
 1500 cal evidence for a non-Poissonian process driving
 1501 the flares does not seem especially overwhelming.
 1502 More quantitatively, the peaks observed at the or-
 1503 bital and synodic periods are within the $\pm 2\sigma$ range
 1504 of a Poissonian process, and those at $P_{\text{orb}} + P_{\text{syn}}$ and
 1505 $P_{\text{orb}} + 2P_{\text{syn}}$ are only slightly above this range. With
 1506 that said, future analyses of these data by investiga-
 1507 tors with more knowledge of this topic could very
 1508 well yield more quantitative insights. Such analy-
 1509 ses should keep in mind an important caveat: the
 1510 amplitude distribution of M-dwarf flares extends
 1511 up to many times the quiescent flux (see Figure 7 of
 1512 Günther et al. 2020). A flare on Kepler 1627B pro-
 1513 ducing double its quiescent white-light flux would
 1514 yield a $\approx 1\%$ apparent amplitude. Such flares could
 1515 represent a significant fraction of those in the Ke-
 1516 pler observations.